Spin excitations in the excitonic spin-density-wave state of the iron pnictides

P. M. R. Brydon* and C. Timm†
Institut für Theoretische Physik, Technische Universität Dresden, 01062 Dresden, Germany
(Received 8 September 2009; revised manuscript received 8 October 2009; published 3 November 2009)

Motivated by the iron pnictides, we examine the spin excitations in an itinerant antiferromagnet where a spin-density wave (SDW) originates from an excitonic instability of nested electronlike and holelike Fermi pockets. Using the random-phase approximation, we derive the Dyson equation for the transverse susceptibility in the excitonic SDW state. The Dyson equation is solved for two different two-band models, describing an antiferromagnetic insulator and metal, respectively. We determine the collective spin-wave dispersions and also consider the single-particle continua. The results for the excitonic models are compared with each other and also contrasted with the well-known SDW state of the Hubbard model. Despite the qualitatively different SDW states in the two excitonic models, their magnetic response shows many similarities. We conclude with a discussion of the relevance of the excitonic SDW scenario to the iron pnictides.

DOI: 10.1103/PhysRevB.80.174401 PACS number(s): 75.30.Fv, 75.10.Lp

I. INTRODUCTION

The recent discovery of superconductivity in iron pnictides has sparked a tremendous research effort.[1,2] The remarkably high superconducting transition temperature T_c of some of these compounds,[3] their layered quasi-two-dimensional (2D) structure,[4] the proximity of superconductivity and antiferromagnetism in their phase diagrams,[5–8] and the likely unconventional superconducting pairing state[9–13] are reminiscent of the cuprates.[14] It is a tantalizing prospect that the iron pnictides can shed light onto the problem of unconventional high-T_c superconductivity in general.

For this it is essential to assess the differences between the cuprates and the iron pnictides. For example, the pnictides have a much more complicated Fermi surface.[15] The antiferromagnetic states in the two families are also qualitatively different. In the cuprates, superconductivity appears by doping an insulating antiferromagnetic parent compound. The pnictide parent compounds RFeAsO (R is a rare-earth ion) and $A\mathrm{Fe}_2\mathrm{As}_2$ (A is an alkaline-earth ion) are also antiferromagnets but there is compelling evidence that they display a metallic spin-density-wave (SDW) state: the value of the magnetic moment at the Fe sites is small,[6,7,16] the compounds display metallic transport properties below the Néel temperature T_N,[16–18] and angle resolved photoemission spectroscopy (ARPES) and quantum oscillation experiments find a reconstructed Fermi surface below T_N.[19,20]

The electron-phonon interaction in the pnictides is much too weak to account for the high-T_c values.[21] Instead, the most likely candidate for the "glue" binding the electrons into Cooper pairs are spin fluctuations,[11–13] which are enhanced by the proximity to the SDW state. A proper understanding of the SDW phase is therefore likely the key to the physics of the pnictides. Intriguingly, *ab initio* calculations suggest that the nesting of electron and hole Fermi pockets is responsible for the SDW,[15] indicating that, like the superconductivity, the antiferromagnetism of these compounds has a multiband character. The best known material where a SDW arises from such a nesting property is chromium[22–26] and this mechanism has also been implicated for manganese alloys.[27]

The SDW in these compounds belongs to a broader class of density-wave states. Consider a material with electronlike and holelike Fermi pockets separated by a nesting vector $\mathbf{Q}$ in the presence of interband Coulomb repulsion. Performing a particle-hole transformation on one of the bands, we obtain an attractive interaction between the particles in one band and the holes in the other. Within a BCS-type mean-field theory, the attractive interaction causes the condensation of interband electron-hole pairs (excitons) with relative wave vector $\mathbf{Q}$, thereby opening a gap in the single-particle excitation spectrum.[28] Although the interband Coulomb repulsion causes the excitonic instability, additional interband scattering terms are required to stabilize one of several different density-wave states, such as a SDW or a charge-density wave (CDW).[29–31]

Several authors have discussed the SDW state of the pnictides in terms of an excitonic instability of nested electron and hole Fermi pockets without regard to the orbital origin of these bands.[31–36] An alternative school of thought emphasizes the importance of the complicated mixing of the iron $3d$ orbitals at the Fermi energy and of the various interorbital interactions.[37–40] These two approaches are not contradictory, however, since the excitonic model can be understood as an effective low-energy theory for the orbital models.[31,34] Furthermore, even in an orbital model, the SDW state is still driven by the nesting of electron and hole Fermi pockets. Indeed, at the mean-field level all these models yield qualitatively identical conclusions. A conceptually different picture based on the ordering of localized moments has also been proposed.[11,41–43] Although it is hard to reconcile with the observed metallic properties[16,17] and the moderate interaction strengths,[44,45] this picture is consistent with several neutron-scattering experiments.[46,47] At present, it is difficult to discriminate between the itinerant (excitonic) and localized scenarios, as the dynamical spin response of the itinerant models is unknown. It is therefore desirable to determine the spin excitations in the excitonic SDW model.

It is the purpose of this paper to examine the transverse spin susceptibility within the excitonic SDW state of a general two-band model. We work within the limits of weak to moderate correlation strength, using the random-phase approximation (RPA) to construct the Dyson equation for the susceptibility. In order to understand the generic features of the spin excitations in the excitonic SDW state, we calculate

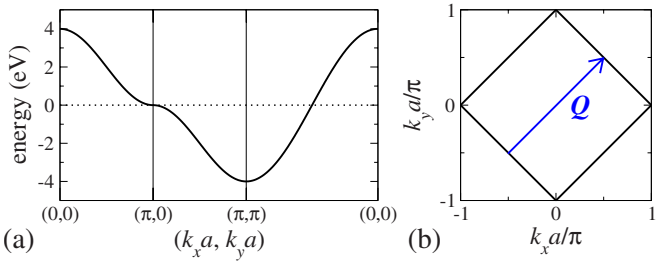

FIG. 1. (Color online) (a) Band structure and (b) Fermi surface of the Hubbard model for $U=0$. In (b), the nesting vector $\mathbf{Q}=(\pi/a,\pi/a)$ is also shown.

the RPA susceptibilities for the simplest model showing this instability. We pay particular attention to the spin waves (magnons) and damped paramagnons. In the simplest model, however, the SDW state is insulating. We therefore verify the robustness of our results by applying our theory to a system where portions of the Fermi surface remain ungapped in the SDW phase, as in the iron pnictides. We contrast our results for the excitonic SDW state with those for the SDW phase of the single-band Hubbard model, which is commonly used to describe the antiferromagnetic state of the cuprates.

The structure of this paper is as follows. We commence in Sec. II with a brief review of the RPA-level results for the transverse susceptibility in the SDW state of the Hubbard model.[48–50] We then proceed in Sec. III with a general discussion of the excitonic SDW state in a two-band model and present the Dyson equation for the transverse susceptibilities. The RPA susceptibility and spin-wave dispersion is then calculated for the insulating and metallic excitonic SDW models in Secs. III A and III B, respectively. All presented results are calculated in the limit of zero temperature. In order to properly compare the different models, we choose interaction strengths such that the zero-temperature SDW gap is the same. We conclude with a comparison with experimental results in Sec. IV and a summary of our work in Sec. V.

II. HUBBARD MODEL

The Hamiltonian of the Hubbard model reads

$$H=\sum_{\mathbf{k},\sigma}\epsilon_{\mathbf{k}}c^{\dagger}_{\mathbf{k},\sigma}c_{\mathbf{k},\sigma}+\frac{U}{V}\sum_{\mathbf{k},\mathbf{k}',\mathbf{q}}c^{\dagger}_{\mathbf{k}+\mathbf{q},\uparrow}c_{\mathbf{k},\uparrow}c^{\dagger}_{\mathbf{k}'-\mathbf{q},\downarrow}c_{\mathbf{k}',\downarrow}, \quad (1)$$

where $c^{\dagger}_{\mathbf{k},\sigma}$ ($c_{\mathbf{k},\sigma}$) creates (destroys) an electron with momentum $\mathbf{k}$ and spin σ. We assume a 2D nearest-neighbor tight-binding dispersion $\epsilon_{\mathbf{k}}=-2t(\cos k_x a+\cos k_y a)$, where a is the lattice constant. We plot the band structure $\epsilon_{\mathbf{k}}$ and the resulting Fermi surface at half filling in Figs. 1(a) and 1(b), respectively.

At half filling and sufficiently low temperature T, the Hubbard model is unstable toward a SDW state with nesting vector $\mathbf{Q}=(\pi/a,\pi/a)$, which connects opposite sides of the Fermi surface. We assume a SDW polarized along the z axis and decouple the interaction term in Eq. (1) by introducing the SDW gap

$$\Delta=\frac{U}{V}{\sum_{\mathbf{k},\sigma}}'\sigma\langle c^{\dagger}_{\mathbf{k}+\mathbf{Q},\sigma}c_{\mathbf{k},\sigma}\rangle. \quad (2)$$

The primed sum denotes summation only over the reduced, magnetic Brillouin zone. Diagonalizing the mean-field Hamiltonian, we find two bands in the reduced Brillouin zone with energies $E_{\pm,\mathbf{k}}=\pm\sqrt{\epsilon^2_{\mathbf{k}}+\Delta^2}$. In the following, we will assume $t=1$ eV and $U=0.738$ eV, which gives a critical temperature for the SDW state of $T_{\mathrm{SDW}}=138$ K and a $T=0$ gap $\Delta=21.3$ meV.

The dynamical spin susceptibility is defined by

$$\chi_{ij}(\mathbf{q},\mathbf{q}';i\omega_n)=\frac{1}{V}\int_0^{\beta}d\tau\langle T_{\tau}S^i(\mathbf{q},\tau)S^j(-\mathbf{q}',0)\rangle e^{i\omega_n\tau}, \quad (3)$$

where T_{τ} is the time-ordering operator and

$$S^i(\mathbf{q},\tau)=\frac{1}{\sqrt{V}}\sum_{\mathbf{k}}\sum_{s,s'}c^{\dagger}_{\mathbf{k}+\mathbf{q},s}(\tau)\frac{\sigma^i_{s,s'}}{2}c_{\mathbf{k},s'}(\tau). \quad (4)$$

Because of the doubling of the unit cell in the SDW state, the susceptibility in Eq. (3) is nonzero for $\mathbf{q}=\mathbf{q}'$ and $\mathbf{q}=\mathbf{q}'+\mathbf{Q}$, the latter referred to as the umklapp susceptibility.[48] Both appear in the ladder diagrams for the transverse susceptibility, yielding the Dyson equation

$$\begin{aligned}\chi_{-+}(\mathbf{q},\mathbf{q}';i\omega_n)=&\,\delta_{\mathbf{q},\mathbf{q}'}\chi^{(0)}_{-+}(\mathbf{q},\mathbf{q};i\omega_n)\\&+\delta_{\mathbf{q}+\mathbf{Q},\mathbf{q}'}\chi^{(0)}_{-+}(\mathbf{q},\mathbf{q}+\mathbf{Q};i\omega_n)\\&+U\chi^{(0)}_{-+}(\mathbf{q},\mathbf{q};i\omega_n)\chi_{-+}(\mathbf{q},\mathbf{q}';i\omega_n)\\&+U\chi^{(0)}_{-+}(\mathbf{q},\mathbf{q}+\mathbf{Q};i\omega_n)\chi_{-+}(\mathbf{q}+\mathbf{Q},\mathbf{q}';i\omega_n),\end{aligned} \quad (5)$$

where the superscript (0) indicates the mean-field susceptibilities. Explicit expressions for $\chi_{-+}(\mathbf{q},\mathbf{q};i\omega_n)$ and $\chi_{-+}(\mathbf{q},\mathbf{q}+\mathbf{Q};i\omega_n)$ can be found in Ref. 50.

We plot the imaginary part of $\chi_{-+}(\mathbf{q},\omega)=\chi_{-+}(\mathbf{q},\mathbf{q};\omega)$ along the line $\mathbf{q}=(q_x,q_y=q_x)$ in Fig. 2. The calculation of the mean-field susceptibilities in the Dyson equation (5) was performed over a $10\,000\times10\,000$ $\mathbf{k}$-point mesh. In the analytic continuation $i\omega_n\to\omega+i\delta$ we assume a finite width $\delta=1$ meV. Smaller values of δ and finer $\mathbf{k}$-point meshes do not produce qualitative or significant quantitative changes in our results.

Im $\chi_{-+}(\mathbf{q},\omega)$ in Fig. 2 displays very different behavior for energies $\omega<2\Delta=42.6$ meV and $\omega>2\Delta$. In the former region, the dispersion of the collective spin waves is clearly visible as the sharp dark line. The finite width of this line is a consequence of the broadening δ. The dispersion is almost flat for $0.1\pi/a\lesssim q_x=q_y\lesssim0.9\pi/a$, where it lies very close to $\omega=2\Delta$. The distribution of spectral weight for the spin wave is asymmetric, with much greater weight close to $\mathbf{q}=\mathbf{Q}$ than

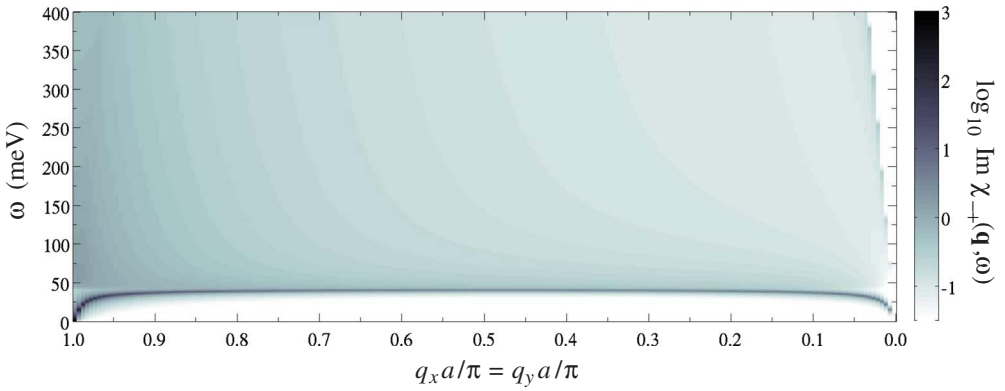

FIG. 2. (Color online) Imaginary part of the transverse susceptibility in the Hubbard model for $\mathbf{q}=(q_x,q_y=q_x)$. The spin-wave dispersion is visible as the dark line running across the figure at $\omega<2\Delta=42$ meV. Note the logarithmic color scale.

at $\mathbf{q}=0$, reflecting the suppression of long-wavelength spin excitations in the SDW state.[51]

For $\omega>2\Delta$, we find a continuum of excitations. It starts abruptly at $\omega=2\Delta$, corresponding to the minimum energy for a single-particle excitation across the SDW gap. This minimum is the same at all $\mathbf{k}$ points lying on the Fermi surface shown in Fig. 1(b). By inspection, we see that for every value of $\mathbf{q}$, there exist points $\mathbf{k}$ and $\mathbf{k}+\mathbf{q}$ lying on the Fermi surface so that the minimum energy required for any excitation is $\omega=2\Delta$. We also see that Im $\chi_{-+}(\mathbf{q},\omega)$ tends to decrease with increasing ω. This can be understood in terms of the density of states (DOS) in the noninteracting model: the DOS has a van Hove singularity at the Fermi energy and decreases monotonically as one moves to higher or lower energies. For an occupied state with energy ω_o below the Fermi energy, the density of unoccupied states with energy ω_u above the Fermi energy therefore decreases with increasing $\omega=\omega_u-\omega_o$ and hence the "density of excitations" contributing to the transverse susceptibility also decreases with increasing ω.

Close to $\mathbf{q}=0$, the continuum is bounded from above by the line $\omega=\mathbf{v}_F\cdot\mathbf{q}$, where $\mathbf{v}_F$ is the Fermi velocity along $\mathbf{k}=(k_x,k_y=k_x)$. The peak in Im $\chi_{-+}(\mathbf{q},\omega)$ at this edge of the continuum is due to single-particle excitations across the Fermi energy in the same branch of the band structure. A rather weak dispersing feature also appears within the continuum near $\mathbf{q}=\mathbf{Q}$, as shown in more detail in Fig. 3. This paramagnon originates from single-particle excitations into the back-folded band. Like the feature at small $\mathbf{q}$, the paramagnon disperses with the Fermi velocity. The paramagnon and spin-wave dispersions curve away from one another in what appears to be an avoided crossing.

Solving Eq. (5) for $\chi_{-+}(\mathbf{q},\mathbf{q};i\omega_n)$ requires the inversion of a 2×2 matrix. The determinant $\mathcal{D}(\mathbf{q},i\omega_n)$ of this matrix is

$$\mathcal{D}(\mathbf{q},i\omega_n)=[1-U\chi^{(0)}_{-+}(\mathbf{q},\mathbf{q};i\omega_n)]\times[1-U\chi^{(0)}_{-+}(\mathbf{q}+\mathbf{Q},\mathbf{q}+\mathbf{Q};i\omega_n)]-[U\chi^{(0)}_{-+}(\mathbf{q},\mathbf{q}+\mathbf{Q};i\omega_n)]^2. \quad (6)$$

Making the analytic continuation $i\omega_n\rightarrow\omega+i0^+$, the solution of Re $\mathcal{D}(\mathbf{q},\omega)=0$ yields the spin-wave dispersion. At low energies, it has a linear dependence upon $\delta\mathbf{q}=\mathbf{Q}-\mathbf{q}$, i.e., $\omega=c_{\mathrm{SW}}|\delta\mathbf{q}|$, where c_{SW} is the spin-wave velocity. An expression for c_{SW} is obtained by expanding $\mathcal{D}(\mathbf{q},\omega)$ about $\mathbf{q}=\mathbf{Q}$ and $\omega=0$.[48–50] In agreement with Ref. 49, we find

$$c_{\mathrm{SW}}=\sqrt{\frac{-4(1/U-\Delta^2 x)t^2\gamma}{x/U}}, \quad (7)$$

where

$$x=\frac{1}{V}\sum_{\mathbf{k}}{}'\frac{1}{E^3_{\mathbf{k}}}, \quad (8)$$

$$\gamma=\frac{1}{V}\sum_{\mathbf{k}}{}'\left\{\frac{1}{E^3_{\mathbf{k}}}(\cos^2 k_x a+\cos k_x a\cos k_y a)+\frac{\epsilon^2_{\mathbf{k}}-2\Delta^2}{E^5_{\mathbf{k}}}\sin^2 k_x a\right\}. \quad (9)$$

The spin-wave velocity is plotted as a function of U in Fig. 4(a) while we compare the low-energy linearized form of the spin-wave dispersion to the numerically determined result in Fig. 4(b). As can be seen, the linearized result holds only for small energies $\omega\lesssim0.5\Delta$.

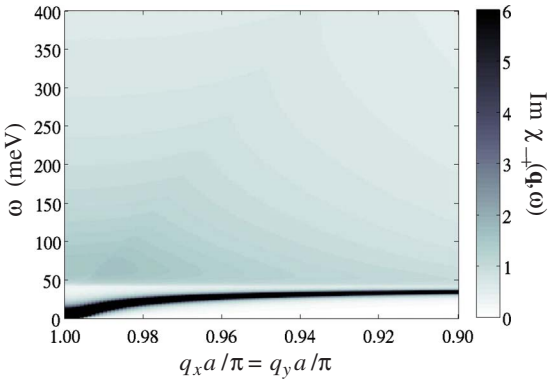

FIG. 3. (Color online) Imaginary part of the transverse spin susceptibility in the Hubbard model for $\mathbf{q}=(q_x,q_y=q_x)$ close to $\mathbf{Q}$. Note the linear color scale.

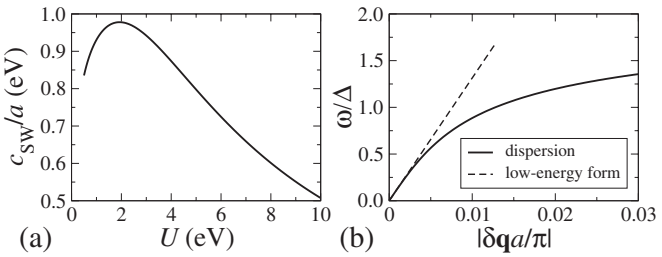

FIG. 4. (a) Spin-wave velocity c_{SW} in the Hubbard model as a function of U for $t=1$ eV. (b) Comparison of the spin-wave dispersion and the low-energy linear form as a function of $\delta\mathbf{q}=\mathbf{Q}-\mathbf{q}$ for $U=0.738$ eV.

III. EXCITONIC MODEL

In this section we discuss the excitonic SDW in a general two-band model with Fermi-surface nesting. We begin by outlining the known results for the mean-field SDW state.[24,25,28–30] We write the Hamiltonian as

$$H = H_0 + H_I, \tag{10}$$

where the noninteracting system is described by

$$H_0 = \sum_{\mathbf{k}} \sum_{\sigma} [(\epsilon^c_{\mathbf{k}} - \mu) c^\dagger_{\mathbf{k}\sigma} c_{\mathbf{k}\sigma} + (\epsilon^f_{\mathbf{k}} - \mu) f^\dagger_{\mathbf{k}\sigma} f_{\mathbf{k}\sigma}] \tag{11}$$

and $c^\dagger_{\mathbf{k},\sigma}$ ($f^\dagger_{\mathbf{k},\sigma}$) creates an electron with spin σ and momentum $\mathbf{k}$ in the electronlike c band (holelike f band). The second term in Eq. (10) describes the interactions in the model system. Following Refs. 31 and 34, we take this to consist of five on-site terms $H_I=H_{cc}+H_{ff}+H_{cf}+H_{\mathrm{ITa}}+H_{\mathrm{ITb}}$ that arise naturally in the low-energy effective theory of a multiorbital model. These correspond to intraband Coulomb repulsion,

$$H_{cc} = \frac{g_{cc}}{V} \sum_{\mathbf{k},\mathbf{k}',\mathbf{q}} c^\dagger_{\mathbf{k}+\mathbf{q},\uparrow} c_{\mathbf{k},\uparrow} c^\dagger_{\mathbf{k}'-\mathbf{q},\downarrow} c_{\mathbf{k}',\downarrow}, \tag{12}$$

$$H_{ff} = \frac{g_{ff}}{V} \sum_{\mathbf{k},\mathbf{k}',\mathbf{q}} f^\dagger_{\mathbf{k}+\mathbf{q},\uparrow} f_{\mathbf{k},\uparrow} f^\dagger_{\mathbf{k}'-\mathbf{q},\downarrow} f_{\mathbf{k}',\downarrow}, \tag{13}$$

interband Coulomb repulsion,

$$H_{cf} = \frac{g_{cf}}{V} \sum_{\mathbf{k},\mathbf{k}',\mathbf{q}} \sum_{\sigma,\sigma'} c^\dagger_{\mathbf{k}+\mathbf{q},\sigma} c_{\mathbf{k},\sigma} f^\dagger_{\mathbf{k}'-\mathbf{q},\sigma'} f_{\mathbf{k}',\sigma'}, \tag{14}$$

and two distinct types of correlated interband transitions,

$$H_{\mathrm{ITa}} = \frac{g_{2a}}{V} \sum_{\mathbf{k},\mathbf{k}',\mathbf{q}} (c^\dagger_{\mathbf{k}+\mathbf{q},\uparrow} c^\dagger_{\mathbf{k}'-\mathbf{q},\downarrow} f_{\mathbf{k}',\downarrow} f_{\mathbf{k},\uparrow} + \mathrm{H.c.}), \tag{15}$$

$$H_{\mathrm{ITb}} = \frac{g_{2b}}{V} \sum_{\mathbf{k},\mathbf{k}',\mathbf{q}} \sum_{\sigma,\sigma'} c^\dagger_{\mathbf{k}+\mathbf{q},\sigma} f^\dagger_{\mathbf{k}'-\mathbf{q},\sigma'} c_{\mathbf{k}',\sigma'} f_{\mathbf{k},\sigma}. \tag{16}$$

The interband interaction terms are responsible for a density-wave instability when the electron and hole Fermi pockets are sufficiently close to nesting. A number of different density-wave states are possible:[30] a CDW with effective coupling constant $g_{\mathrm{CDW}}=g_{cf}-g_{2a}-2g_{2b}$, a SDW with coupling $g_{\mathrm{SDW}}=g_{cf}+g_{2a}$, a charge-current-density wave (CCDW) with $g_{\mathrm{CCDW}}=g_{cf}+g_{2a}-2g_{2b}$, and a spin-current-density wave (SCDW) with $g_{\mathrm{SCDW}}=g_{cf}-g_{2a}$. In order to model the iron pnictides, we henceforth assume that the SDW state has the largest coupling constant.

In the presence of a SDW polarized along the z axis and with nesting vector $\mathbf{Q}$, the effective mean-field Hamiltonian is written as

$$H_{\mathrm{MF}} = H_0 + \sum_{\mathbf{k}} \sum_{\sigma} \sigma\Delta (c^\dagger_{\mathbf{k},\sigma} f_{\mathbf{k}+\mathbf{Q},\sigma} + \mathrm{H.c.}), \tag{17}$$

where the excitonic gap

$$\Delta = \frac{g_{\mathrm{SDW}}}{2V} \sum_{\mathbf{k}} \sum_{\sigma} \sigma \langle c^\dagger_{\mathbf{k},\sigma} f_{\mathbf{k}+\mathbf{Q},\sigma} \rangle \tag{18}$$

is assumed to be real. The precise relationship between Δ and the magnetization is somewhat complicated.[29,30] To elucidate it, we define the field operator,

$$\psi_\sigma(\mathbf{r}) = \frac{1}{\sqrt{V}} \sum_{\mathbf{k}} [\varphi_{\mathbf{k},c}(\mathbf{r}) c_{\mathbf{k},\sigma} + \varphi_{\mathbf{k},f}(\mathbf{r}) f_{\mathbf{k},\sigma}] e^{i\mathbf{k}\cdot\mathbf{r}}, \tag{19}$$

where $\varphi_{\mathbf{k},\alpha}(\mathbf{r})$ is a Bloch function for the band α. The local magnetization $\mathbf{M}(\mathbf{r})$ is then

$$\mathbf{M}(\mathbf{r}) = -\frac{g\mu_B}{V} \sum_{s,s'} \sum_{\mathbf{k},\mathbf{k}'} \sum_{a,b=c,f} \varphi^*_{\mathbf{k},a}(\mathbf{r}) \varphi_{\mathbf{k}',b}(\mathbf{r}) \times e^{-i(\mathbf{k}-\mathbf{k}')\cdot\mathbf{r}} \left\langle a^\dagger_{\mathbf{k},s} \frac{\boldsymbol{\sigma}_{s,s'}}{2} b_{\mathbf{k}',s'} \right\rangle, \tag{20}$$

where g is the g-factor and μ_B is the Bohr magneton. Only in the limit when $\varphi_{\mathbf{k},\alpha}(\mathbf{r})$ is constant do we find Δ to be simply related to the magnetization,

$$\mathbf{M}(\mathbf{r}) = -\frac{2g\mu_B\Delta}{g_{\mathrm{SDW}}} (\cos \mathbf{Q}\cdot\mathbf{r}) \mathbf{e}_z. \tag{21}$$

For simplicity, we follow Refs. 13, 23, 27, and 52 in assuming constant Bloch functions.

In calculating the susceptibilities, we make use of the single-particle Green's functions of the mean-field SDW state. The two normal (diagonal in band indices) Green's functions are defined by

$$G^{cc}_{\mathbf{k},\sigma}(i\omega_n) = -\int_0^\beta d\tau \langle T_\tau c_{\mathbf{k},\sigma}(\tau) c^\dagger_{\mathbf{k},\sigma}(0) \rangle e^{i\omega_n\tau} = \frac{i\omega_n - \epsilon^f_{\mathbf{k}+\mathbf{Q}}}{(i\omega_n - E_{+,\mathbf{k}+\mathbf{Q}})(i\omega_n - E_{-,\mathbf{k}+\mathbf{Q}})}, \tag{22}$$

$$G^{ff}_{\mathbf{k},\sigma}(i\omega_n) = -\int_0^\beta d\tau \langle T_\tau f_{\mathbf{k},\sigma}(\tau) f^\dagger_{\mathbf{k},\sigma}(0) \rangle e^{i\omega_n\tau} = \frac{i\omega_n - \epsilon^c_{\mathbf{k}+\mathbf{Q}}}{(i\omega_n - E_{+,\mathbf{k}})(i\omega_n - E_{-,\mathbf{k}})} \tag{23}$$

while the anomalous (band-mixing) Green's functions are

$$G^{fc}_{\mathbf{k},\sigma}(i\omega_n) = -\int_0^\beta d\tau \langle T_\tau f_{\mathbf{k},\sigma}(\tau) c^\dagger_{\mathbf{k}+\mathbf{Q},\sigma}(0)\rangle e^{i\omega_n\tau} = \frac{\sigma\Delta}{(i\omega_n - E_{+,\mathbf{k}})(i\omega_n - E_{-,\mathbf{k}})}, \tag{24}$$

$$G^{cf}_{\mathbf{k},\sigma}(i\omega_n) = -\int_0^\beta d\tau \langle T_\tau c_{\mathbf{k},\sigma}(\tau) f^\dagger_{\mathbf{k}+\mathbf{Q},\sigma}(0)\rangle e^{i\omega_n\tau} = G^{fc}_{\mathbf{k}+\mathbf{Q},\sigma}(i\omega_n). \tag{25}$$

The functions $E_{\pm,\mathbf{k}}$ are the dispersion relations for the reconstructed bands,

$$E_{\pm,\mathbf{k}} = \frac{1}{2}[\epsilon^c_{\mathbf{k}+\mathbf{Q}} + \epsilon^f_{\mathbf{k}} \pm \sqrt{(\epsilon^c_{\mathbf{k}+\mathbf{Q}} - \epsilon^f_{\mathbf{k}})^2 + 4\Delta^2}]. \tag{26}$$

For energies much larger than Δ we have $E_{+,\mathbf{k}} \approx \epsilon^c_{\mathbf{k}+\mathbf{Q}}$ and $E_{-,\mathbf{k}} \approx \epsilon^f_{\mathbf{k}}$.

The total spin operator is written as

$$\mathbf{S}(\mathbf{r}) = \sum_{s,s'} \psi^\dagger_s(\mathbf{r}) \frac{\boldsymbol{\sigma}_{s,s'}}{2} \psi_{s'}(\mathbf{r}) = \frac{1}{2V} \sum_{a,b=c,f} \sum_{\mathbf{k},\mathbf{q}} \sum_{s,s'} a^\dagger_{\mathbf{k}+\mathbf{q},s} \boldsymbol{\sigma}_{s,s'} b_{\mathbf{k},s'} e^{-i\mathbf{q}\cdot\mathbf{r}} = \frac{1}{\sqrt{V}} \sum_{a,b=c,f} \sum_{\mathbf{q}} \mathbf{S}_{a,b}(\mathbf{q}) e^{-i\mathbf{q}\cdot\mathbf{r}}, \tag{27}$$

where $\mathbf{S}_{a,b}(\mathbf{q})$ is a generalized spin operator. The dynamical spin susceptibility is then defined by

$$\chi_{ij}(\mathbf{q},\mathbf{q}';i\omega_n) = \frac{1}{V} \sum_{a,b} \sum_{a',b'} \int_0^\beta \langle T_\tau S^i_{a,b}(\mathbf{q},\tau) S^j_{a',b'}(-\mathbf{q}',0)\rangle e^{i\omega_n\tau} = \sum_{a,b} \sum_{a',b'} \chi^{aba'b'}_{ij}(\mathbf{q},\mathbf{q}';i\omega_n). \tag{28}$$

The generalized susceptibilities $\chi^{aba'b'}_{ij}(\mathbf{q},\mathbf{q}';i\omega_n)$ are calculated using the RPA. We are only concerned with the transverse susceptibility, which is obtained by summing the ladder diagrams. This yields the Dyson equation

$$\begin{aligned}
\chi^{aba'b'}_{-+,00} = {} & \delta_{\mathbf{q},\mathbf{q}'}(\delta_{a',b}\delta_{b',a}\chi^{abba(0)}_{-+,00} + \delta_{a',\bar{b}}\delta_{b',\bar{a}}\chi^{ab\bar{b}\bar{a}(0)}_{-+,00}) + \delta_{\mathbf{q}+\mathbf{Q},\mathbf{q}'}(\delta_{a',b}\delta_{b',\bar{a}}\chi^{abb\bar{a}(0)}_{-+,0\mathbf{Q}} + \delta_{a',\bar{b}}\delta_{b',a}\chi^{ab\bar{b}a(0)}_{-+,0\mathbf{Q}}) \\
& + g_{cc}(\chi^{abcc(0)}_{-+,00}\chi^{cca'b'}_{-+,00} + \chi^{abcc(0)}_{-+,0\mathbf{Q}}\chi^{cca'b'}_{-+,\mathbf{Q}0}) + g_{ff}(\chi^{abff(0)}_{-+,00}\chi^{ffa'b'}_{-+,00} + \chi^{abff(0)}_{-+,0\mathbf{Q}}\chi^{ffa'b'}_{-+,\mathbf{Q}0}) \\
& + g_{cf}(\chi^{abcf(0)}_{-+,00}\chi^{fca'b'}_{-+,00} + \chi^{abcf(0)}_{-+,0\mathbf{Q}}\chi^{fca'b'}_{-+,\mathbf{Q}0} + \chi^{abfc(0)}_{-+,00}\chi^{cfa'b'}_{-+,00} + \chi^{abfc(0)}_{-+,0\mathbf{Q}}\chi^{cfa'b'}_{-+,\mathbf{Q}0}) \\
& + g_{2a}(\chi^{abcf(0)}_{-+,00}\chi^{cfa'b'}_{-+,00} + \chi^{abcf(0)}_{-+,0\mathbf{Q}}\chi^{cfa'b'}_{-+,\mathbf{Q}0} + \chi^{abfc(0)}_{-+,00}\chi^{fca'b'}_{-+,00} + \chi^{abfc(0)}_{-+,0\mathbf{Q}}\chi^{fca'b'}_{-+,\mathbf{Q}0}) \\
& + g_{2b}(\chi^{abcc(0)}_{-+,00}\chi^{ffa'b'}_{-+,00} + \chi^{abcc(0)}_{-+,0\mathbf{Q}}\chi^{ffa'b'}_{-+,\mathbf{Q}0} + \chi^{abff(0)}_{-+,00}\chi^{cca'b'}_{-+,00} + \chi^{abff(0)}_{-+,0\mathbf{Q}}\chi^{cca'b'}_{-+,\mathbf{Q}0}),
\end{aligned} \tag{29}$$

where we have adopted the short-hand notation

$$\chi^{aba'b'(0)}_{-+,\mathbf{mn}} = \chi^{aba'b'(0)}_{-+}(\mathbf{q}+\mathbf{m},\mathbf{q}+\mathbf{n};i\omega_n), \tag{30}$$

$$\chi^{aba'b'}_{-+,\mathbf{mn}} = \chi^{aba'b'}_{-+}(\mathbf{q}+\mathbf{m},\mathbf{q}'+\mathbf{n};i\omega_n). \tag{31}$$

Note that $\chi^{aba'b'(0)}_{-+,\mathbf{mn}}$ does not depend on $\mathbf{q}'$. We have also introduced the notation $\bar{a}=c(f)$ when $a=f(c)$. The first line of Eq. (29) gives the mean-field susceptibilities, obtained by using Wick's theorem to contract the correlation function in Eq. (28) into products of two mean-field Green's functions. The first two terms on the right-hand side of Eq. (29) are the correlators resulting from the product of two normal Green's functions,

$$\chi^{abba(0)}_{-+,00} = -\frac{1}{V}\sum_{\mathbf{k}} \frac{1}{\beta}\sum_{i\nu_n} G^{bb}_{\mathbf{k},\uparrow}(i\nu_n) G^{aa}_{\mathbf{k}+\mathbf{q},\downarrow}(i\nu_n - i\omega_n)$$

and from the product of two anomalous Green's functions,

$$\chi^{ab\bar{b}\bar{a}(0)}_{-+,00} = -\frac{1}{V}\sum_{\mathbf{k}} \frac{1}{\beta}\sum_{i\nu_n} G^{b\bar{b}}_{\mathbf{k},\uparrow}(i\nu_n) G^{\bar{a}a}_{\mathbf{k}+\mathbf{q},\downarrow}(i\nu_n - i\omega_n).$$

The next two terms are the umklapp susceptibilities which, as in the Hubbard model, are the product of a normal and an anomalous Green's function,

$$\chi^{abb\bar{a}(0)}_{-+,0\mathbf{Q}} = -\frac{1}{V}\sum_{\mathbf{k}} \frac{1}{\beta}\sum_{i\nu_n} G^{bb}_{\mathbf{k},\uparrow}(i\nu_n) G^{\bar{a}a}_{\mathbf{k}+\mathbf{q},\downarrow}(i\nu_n - i\omega_n),$$

$$\chi^{ab\bar{b}a(0)}_{-+,0\mathbf{Q}} = -\frac{1}{V}\sum_{\mathbf{k}} \frac{1}{\beta}\sum_{i\nu_n} G^{b\bar{b}}_{\mathbf{k},\uparrow}(i\nu_n) G^{aa}_{\mathbf{k}+\mathbf{q},\downarrow}(i\nu_n - i\omega_n).$$

The remaining lines of Eq. (29) give the ladder sums for the various interactions: on the second line we have the intraband Coulomb interactions, on the third line the interband Coulomb interaction, and on the last two lines the two types of correlated transitions. In Figs. 5(a) and 5(b), we show a diagrammatic representation of the Dyson equation for $\chi^{cffc}_{-+,00}$ and $\chi^{cccc}_{-+,00}$, respectively. Note that the Dyson equation is also

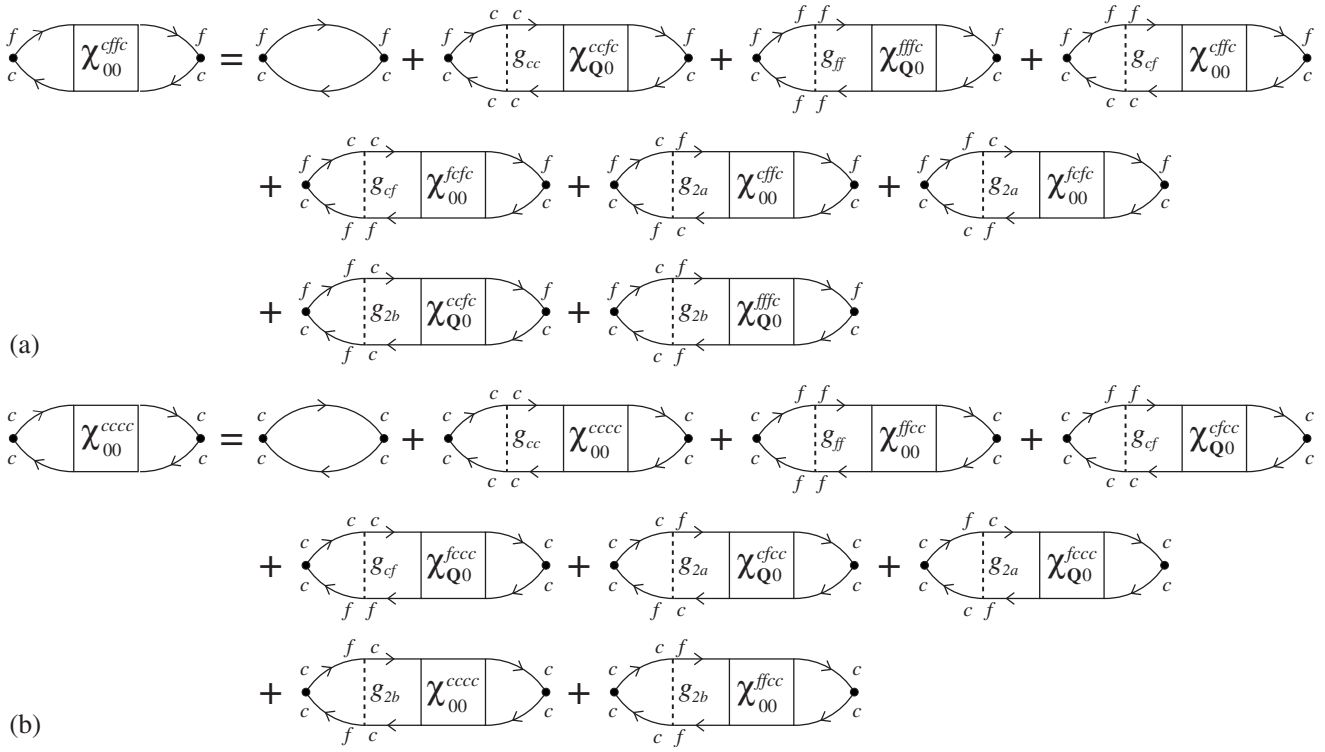

FIG. 5. Diagrammatic representation of the Dyson Eq. (29) for (a) $\chi^{cffc}_{-+,00}$ and (b) $\chi^{cccc}_{-+,00}$. The curved lines are the mean-field Green's functions in the SDW state. When the label $b=c,f$ follows the label $a=c,f$ in the direction of the arrow, the corresponding Green's function is G^{ab}.

valid in the normal state in which case the $\chi^{abba(0)}_{-+,00}$ are the only nonzero mean-field susceptibilities.

From the structure of the Dyson equation, we see that $\chi^{aba'b'}_{-+,\mathbf{mn}}$ is only nonzero for $\mathbf{q}=\mathbf{q}'$ and $\mathbf{m}$, $\mathbf{n}\in\{0,\mathbf{Q}\}$. We observe that Eq. (29) may then be written as four independent sets of coupled equations for

$$\{\chi^{cccc}_{-+,00},\chi^{ffcc}_{-+,00},\chi^{fccc}_{-+,\mathbf{Q}0},\chi^{cfcc}_{-+,\mathbf{Q}0}\}, \tag{32a}$$

$$\{\chi^{ffff}_{-+,00},\chi^{ccff}_{-+,00},\chi^{cfff}_{-+,\mathbf{Q}0},\chi^{fcff}_{-+,\mathbf{Q}0}\}, \tag{32b}$$

$$\{\chi^{fccf}_{-+,00},\chi^{cfcf}_{-+,00},\chi^{cccf}_{-+,\mathbf{Q}0},\chi^{ffcf}_{-+,\mathbf{Q}0}\}, \tag{32c}$$

$$\{\chi^{cffc}_{-+,00},\chi^{fcfc}_{-+,00},\chi^{ccfc}_{-+,\mathbf{Q}0},\chi^{fffc}_{-+,\mathbf{Q}0}\}. \tag{32d}$$

Note that this includes $\chi^{aba'b'}_{-+,\mathbf{mn}}$ for $\mathbf{mn}=\mathbf{QQ}$ and $\mathbf{mn}=0\mathbf{Q}$ by symmetry; all other possible transverse susceptibilities vanish. The first two sets contain the contributions to the intraband susceptibility, which involve spin-flip transitions within the c and f bands,

$$\chi^{\text{intra}}_{-+}(\mathbf{q},i\omega_n)=\frac{1}{V}\sum_{a,b=c,f}\int_0^\beta d\tau\langle T_\tau S^-_{a,a}(\mathbf{q},\tau)S^+_{b,b}(-\mathbf{q},0)\rangle e^{i\omega_n\tau}$$
$$=\chi^{cccc}_{-+,00}+\chi^{ccff}_{-+,00}+\chi^{ffcc}_{-+,00}+\chi^{ffff}_{-+,00}. \tag{33}$$

The last two sets contain the contributions to the interband susceptibility, which involve spin-flip transitions between the c and f bands,

$$\chi^{\text{inter}}_{-+}(\mathbf{q},i\omega_n)=\frac{1}{V}\sum_{a,b=c,f}\int_0^\beta d\tau\langle T_\tau S^-_{a,\bar{a}}(\mathbf{q},\tau)S^+_{b,\bar{b}}(-\mathbf{q},0)\rangle e^{i\omega_n\tau}$$
$$=\chi^{cffc}_{-+,00}+\chi^{cfcf}_{-+,00}+\chi^{fcfc}_{-+,00}+\chi^{fccf}_{-+,00}. \tag{34}$$

We note that the Dyson equation for the interband susceptibilities has been previously obtained in Refs. 23 and 52 for the case where only the interband Coulomb interaction Eq. (14) is nonzero. From Eq. (28) we see that the total transverse susceptibility is the sum of the intraband and interband contributions,

$$\chi_{-+}(\mathbf{q},i\omega_n)=\chi^{\text{intra}}_{-+}(\mathbf{q},i\omega_n)+\chi^{\text{inter}}_{-+}(\mathbf{q},i\omega_n). \tag{35}$$

Since the interband and intraband susceptibilities involve qualitatively different types of excitations, considering these separately offers greater physical insight into the magnetic response than the total susceptibility.

In the following sections we discuss the transverse susceptibility for two different models of the band structure. For simplicity, we restrict ourselves to the case $g_{cc}=g_{ff}=g_{2b}=0$, as these interactions do not drive the SDW instability. We emphasize, however, that the preceeding results are valid for any choice of couplings in both the normal and SDW states. Except where stated otherwise, we furthermore set $g_{2a}=0$, as at reasonable coupling strengths we find very little change in the transverse susceptibility upon varying g_{cf} and g_{2a} while keeping $g_{\text{SDW}}=g_{cf}+g_{2a}$ fixed. Unless explicitly mentioned, we have used a $10\,000\times10\,000$ $\mathbf{k}$-point mesh and a width $\delta=1$ meV to calculate the mean-field susceptibilities.

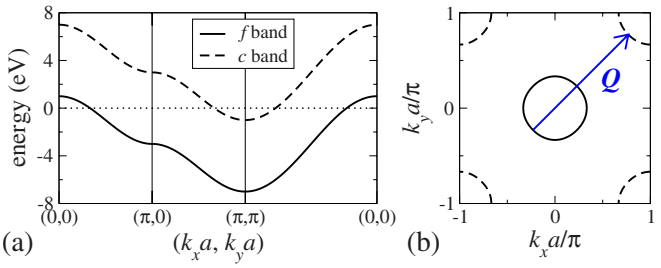

FIG. 6. (Color online) (a) Band structure and (b) Fermi surface of the noninteracting insulating excitonic model. In (b), the nesting vector $\mathbf{Q}=(\pi/a,\pi/a)$ is also shown.

A. Insulating SDW state

We first examine an excitonic model with perfect nesting between the electron and hole bands, i.e., $\epsilon^c_{\mathbf{k}}=-\epsilon^f_{\mathbf{k}+\mathbf{Q}}$ for all $\mathbf{k}$. Although hardly realistic, at the mean-field level it exactly maps onto the BCS model after particle-hole transformation.[28] It is therefore useful for obtaining physically transparent results and is frequently encountered in the literature.[28,29,31,34,35] We assume the 2D band structure

$$\epsilon^c_{\mathbf{k}} = 2t(\cos k_x a + \cos k_y a) + \epsilon_0, \tag{36a}$$

$$\epsilon^f_{\mathbf{k}} = 2t(\cos k_x a + \cos k_y a) - \epsilon_0, \tag{36b}$$

where we set $t=1$ eV and $\epsilon_0=3$ eV. The band structure and Fermi surface at half filling are shown in Figs. 6(a) and 6(b), respectively. Below we will take $g_{\mathrm{SDW}}=1.8$ eV, for which the mean-field equations yield a SDW with nesting vector $\mathbf{Q}=(\pi/a,\pi/a)$, critical temperature $T_{\mathrm{SDW}}=138$ K, and $T=0$ gap $\Delta=21.3$ meV. The system is insulating at $T=0$, with the SDW gap completely removing the Fermi surface.

We plot the imaginary parts of the interband, intraband, and total transverse susceptibilities for $\mathbf{q}=(q_x,q_y=q_x)$ in Figs. 7(a)–7(c), respectively. We consider first the interband contribution. For $\mathbf{q}$ sufficiently close to $\mathbf{Q}$, we find a continuum of single-particle excitations. In contrast to the results for the Hubbard model (Fig. 2), the magnitude of the transverse susceptibility in this region tends to increase with increasing ω. This can again be explained in terms of the DOS of the noninteracting model, which now increases as the energy is raised (lowered) away from the Fermi energy up (down) to a van Hove singularity at 3 eV (−3 eV) in the electronlike (holelike) band. The density of excitations contributing to the susceptibility therefore also increases with ω. As the SDW state is insulating, with a minimum energy of 2Δ required to excite a quasiparticle across the gap, the continuum is sharply bounded at $\omega=2\Delta=42.6$ meV. The continuum is also bounded by a dispersing V-shaped feature with minimum at $\mathbf{q}=0.54\mathbf{Q}$, which is not seen for the Hubbard model. The absence of any weight at small $\mathbf{q}$ is anticipated from the band structure in Fig. 6, which shows that the minimum wave vector for an interband transition with energy $\omega<400$ meV is $\mathbf{q}\approx 0.5\mathbf{Q}$. The V-shaped feature is plotted in detail in Fig. 8(a). As shown in Fig. 8(b), it is due to the weak nesting of the hole band at $\mathbf{k}=0.23\mathbf{Q}$ with the electron band at $\mathbf{k}=0.77\mathbf{Q}$. For the energies considered here, to excellent approximation the interband susceptibility depends only on $|\delta\mathbf{q}|=|\mathbf{Q}-\mathbf{q}|$.

For $\mathbf{q}$ near $\mathbf{Q}$, Fig. 7(a) shows a spin-wave dispersion which appears to intersect the continuum and continue as a paramagnon. Figure 9 reveals, however, that the situation is more complicated: the spin-wave dispersion does not intersect the continuum but instead flattens out as it approaches $\omega=2\Delta$ and disappears at $\mathbf{q}\approx 0.985\mathbf{Q}$. As in the Hubbard model, the paramagnon and spin-wave dispersions appear to avoid one another. The paramagnon nevertheless seems to connect to significant weight lying just inside the continuum region at the intersection point with the spin-wave dispersion.

We now turn our attention to the intraband contribution to the transverse susceptibility in Fig. 7(b). Apart from a forbidden region close to $\mathbf{q}=0$, this appears almost like a mirror image of the interband susceptibility, albeit much reduced in weight. In particular, we note a V-shaped dispersing feature at $\mathbf{q}=0.46\mathbf{Q}$, the tendency of $\mathrm{Im}\,\chi^{\mathrm{intra}}_{-+}(\mathbf{q},\omega)$ to increase with increasing ω, and a dispersing feature at the edge of the $\mathbf{q}\approx 0$ forbidden region, which resembles the paramagnon close to $\mathbf{q}=\mathbf{Q}$. The presence of the V-shaped feature is particularly interesting, as the discussion above indicates that it is due to interband excitations. Thus we find that interband excitations give a significant contribution to the intraband susceptibility. This is confirmed by examining the Dyson equation for $\chi^{cccc}_{-+,00}$, cf. Fig. 5(b): for $g_{cc}=g_{ff}=g_{2\mathrm{b}}=g_{2\mathrm{a}}=0$, as assumed here, the intraband susceptibilities do not appear on the right-hand side of the equation so that the RPA enhancement of $\chi^{cccc}_{-+,00}$ stems only from the umklapp susceptibilities $\chi^{cfcc}_{-+,\mathbf{Q}0}$ and $\chi^{fccc}_{-+,\mathbf{Q}0}$. The coupling to these terms in the Dyson equations is through the anomalous Green's functions G^{cf} and G^{fc}, which reflect the mixing of the states in the electronlike and holelike bands separated by the nesting vector $\mathbf{Q}$ in the SDW phase. Consequently, the intraband susceptibility is similar to the interband susceptibility but shifted by $\mathbf{Q}$.

The total transverse susceptibility in Fig. 7(c) clearly shows the partial symmetry of the response about $\mathbf{q}=\mathbf{Q}/2$ but also the asymmetric distribution of weight. $\mathrm{Im}\,\chi_{-+}(\mathbf{q},\omega)$ for $|\mathbf{q}|<|\mathbf{Q}|/2$ is roughly one order of magnitude smaller than at $\mathbf{q}'=\mathbf{Q}-\mathbf{q}$.

Spin-wave velocity

The calculation of the spin-wave velocity proceeds as for the Hubbard model. For $g_{cc}=g_{ff}=g_{2\mathrm{b}}=0$, solving the Dyson equations for the interband susceptibilities in Eqs. (32c) and (32d) again involves the inversion of a 2×2 matrix, which has the determinant

$$\begin{aligned}\mathcal{D}(\mathbf{q},\omega) = &[1 - g_{cf}\chi^{cfff(0)}_{-+,00} - g_{2\mathrm{a}}\chi^{cfcf(0)}_{-+,00}][1 - g_{cf}\chi^{fccf(0)}_{-+,00} \\ &- g_{2\mathrm{a}}\chi^{fcfc(0)}_{-+,00}] - [g_{cf}\chi^{fcfc(0)}_{-+,00} + g_{2\mathrm{a}}\chi^{fccf(0)}_{-+,00}] \\ &\times [g_{cf}\chi^{cfcf(0)}_{-+,00} + g_{2\mathrm{a}}\chi^{cffc(0)}_{-+,00}].\end{aligned} \tag{37}$$

Expanding this determinant about $\omega=0$ and $\delta\mathbf{q}=\mathbf{Q}-\mathbf{q}=0$, we obtain the low-energy linear form $\omega=c_{\mathrm{SW}}|\delta\mathbf{q}|$ of the spin-wave dispersion. For the band structure considered here, the spin-wave velocity is given by

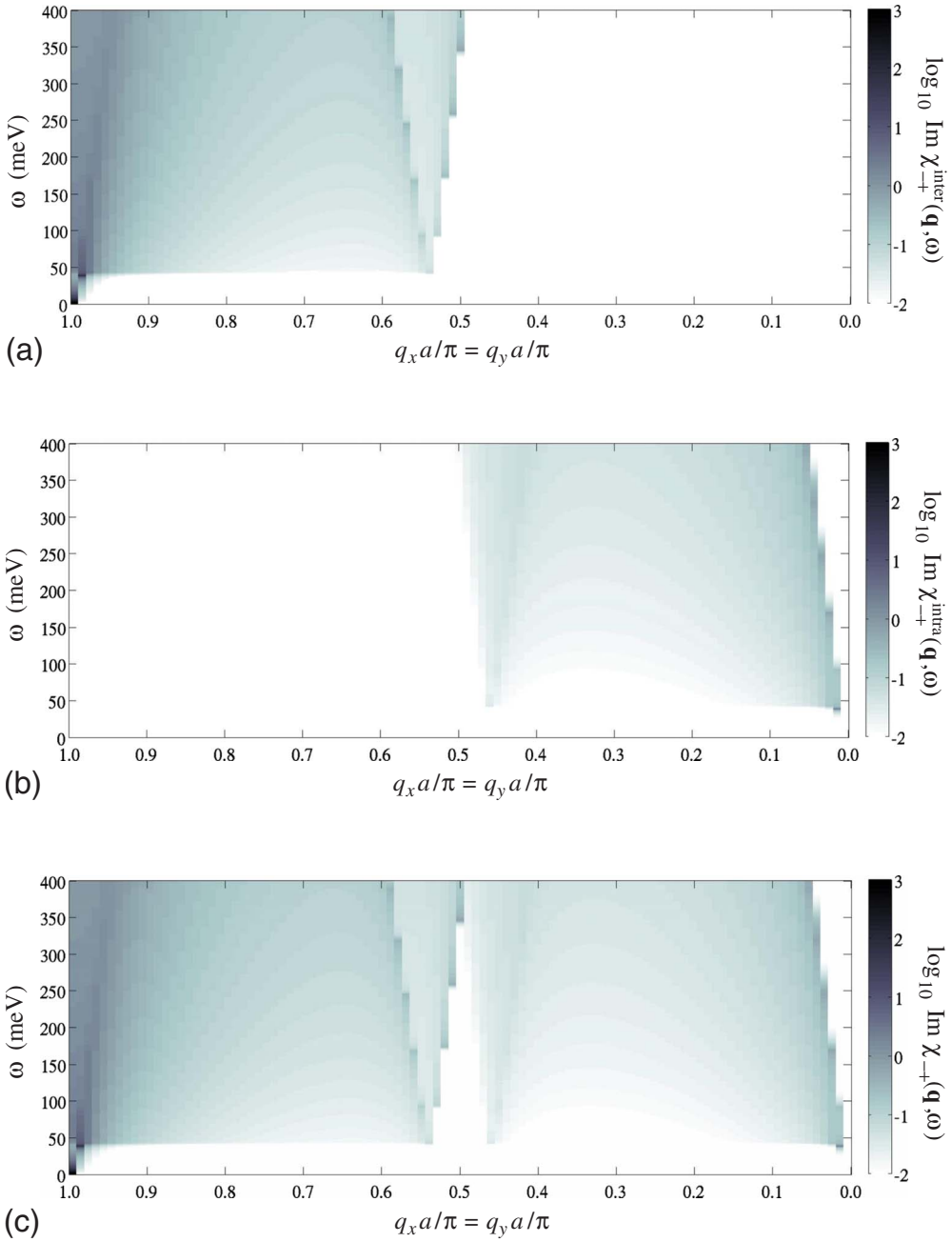

FIG. 7. (Color online) Imaginary part of (a) the interband, (b) the intraband, and (c) the total transverse susceptibility in the insulating excitonic model for $\mathbf{q}=(q_x,q_y=q_x)$. The spin-wave dispersion is visible as the dark line at $\omega<2\Delta$ close to $\mathbf{Q}$ in (a) and (c). Note the logarithmic color scale.

$$c_{\text{SW}} = \sqrt{\frac{2t^2 a_3[a_0(g_{2\text{a}}^2 - g_{cf}^2) - g_{2\text{a}}]}{(a_1^2 + 2a_0 a_2)(g_{2\text{a}}^2 - g_{cf}^2) - 2a_2 g_{2\text{a}}}}, \tag{38}$$

where

$$a_0 = \frac{1}{4V}\sum_{\mathbf{k}} \frac{\Delta^2}{E_{\mathbf{k}}^3}, \quad a_1 = \frac{1}{4V}\sum_{\mathbf{k}} \frac{\epsilon^c_{\mathbf{k}+\mathbf{Q}}}{E_{\mathbf{k}}^3}, \tag{39}$$

$$a_2 = \frac{1}{8V}\sum_{\mathbf{k}} \frac{1}{E_{\mathbf{k}}^3}, \tag{40}$$

$$a_3 = \frac{1}{2V}\sum_{\mathbf{k}} \left\{ \frac{\epsilon^c_{\mathbf{k}+\mathbf{Q}}}{4E_{\mathbf{k}}^3} t \cos k_x a + \frac{2\Delta^4 + \Delta^2(\epsilon^c_{\mathbf{k}+\mathbf{Q}})^2 - (\epsilon^c_{\mathbf{k}+\mathbf{Q}})^4}{E_{\mathbf{k}}^5} \sin^2 k_x a \right\}, \tag{41}$$

and

$$E_{\mathbf{k}} = \sqrt{(\epsilon^c_{\mathbf{k}+\mathbf{Q}})^2 + \Delta^2}. \tag{42}$$

We plot c_{SW} as a function of g_{SDW} for different values of g_{cf} in Fig. 10(a). The behavior of the spin-wave velocity for

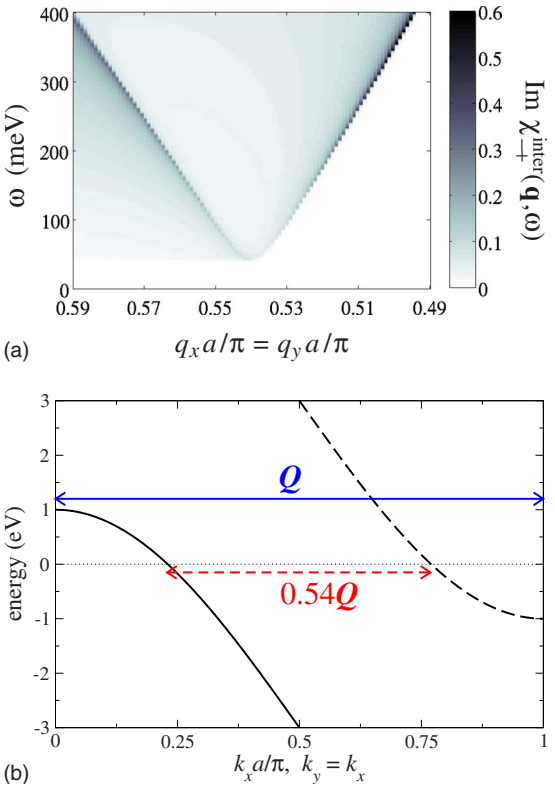

FIG. 8. (Color online) (a) Imaginary part of the interband transverse susceptibility in the insulating excitonic model for $\mathbf{q}=(q_x, q_y=q_x)$ close to $0.54\mathbf{Q}$. Note the linear color scale. (b) Band structure along the Brillouin-zone diagonal, showing the nesting responsible for the dispersing feature in (a).

$g_{\text{SDW}} \gg t$ is included as an inset. For $g_{\text{SDW}} \geq g_{cf}$ we always find $c_{\text{SW}}^2 > 0$; for sufficiently large $g_{cf} > g_{\text{SDW}}$, however, we have $c_{\text{SW}}^2 < 0$ which indicates that the system becomes unstable toward a different ground state. This is not surprising, as for $g_{cf} > g_{\text{SDW}} > 0 > g_{2a}$ the effective coupling g_{SDW} is smaller than that for the CDW or SCDW. In the opposite case $g_{2a} > g_{\text{SDW}} > 0 > g_{cf}$ the coupling constants for the SDW and CCDW states are equal and always greater than those for the CDW and SCDW, and so the SDW remains stable. In

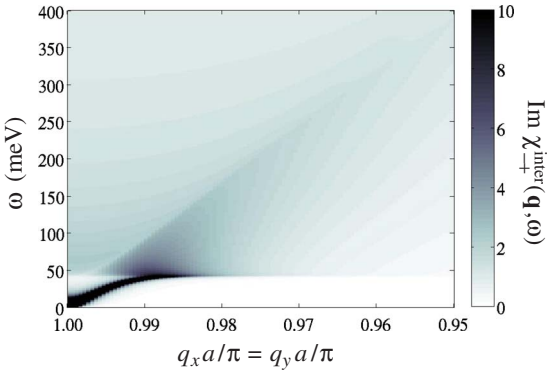

FIG. 9. (Color online) Imaginary part of the interband transverse susceptibility in the insulating excitonic model for $\mathbf{q}=(q_x, q_y=q_x)$ close to $\mathbf{Q}$. The spin-wave dispersion is visible as the thick black line in the lower left-hand corner. Note the linear color scale.

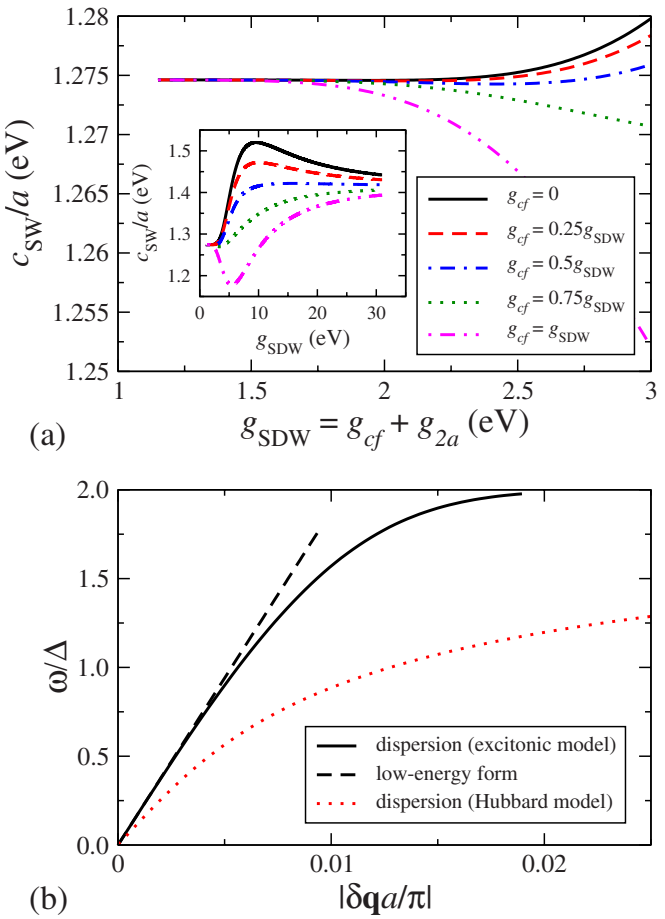

FIG. 10. (Color online) (a) Spin-wave velocity c_{SW} as a function of $g_{\text{SDW}}=g_{cf}+g_{2a}$ in the insulating excitonic model. Inset: c_{SW} for a larger range of g_{SDW}. (b) Spin-wave dispersion in the excitonic model and its low-energy linear form for $g_{\text{SDW}}=1.8$ eV as a function of $\delta\mathbf{q}=\mathbf{q}-\mathbf{Q}$. Shown for comparison is the spin-wave dispersion in the Hubbard model from Fig. 4(b) for the same $T=0$ gap.

Fig. 10(b) we plot the spin-wave dispersion in the excitonic model as a function of $\delta\mathbf{q}$. Compared to a Hubbard model with identical $T=0$ gap, the spin-wave dispersion has both a higher low-energy velocity and remains approximately linear up to higher energies [see Fig. 4(b)].

Although Eq. (38) is a rather complicated function of g_{cf} and g_{2a}, for $g_{\text{SDW}} < 3$ eV the spin-wave velocity in the excitonic model shows remarkably little dependence upon the interaction constants, in contrast to the Hubbard model results in Fig. 4(a). Instead, the value of c_{SW} is fixed by the band structure: for an excitonic gap $\Delta \ll t$ (the weak-coupling limit) we have to excellent approximation $c_{\text{SW}} \approx \tilde{v}_F/\sqrt{2}$ where $\tilde{v}_F$ is the average Fermi velocity. This is anticipated by the results of Refs. 22 and 23 for chromium, where it was found that $c_{\text{SW}}=\sqrt{v_e v_h}/3$, where $v_{e(h)}$ is the electron (hole) Fermi velocity and the factor of $1/\sqrt{3}$ arises because a three-dimensional Fermi surface is considered. It is also consistent with our observation that $\chi_{-+}(\mathbf{q},\omega)$ is rather insensitive to the choice of g_{cf} and g_{2a} for small g_{SDW}.

The behavior of c_{SW} in the strong-coupling regime of the Hubbard and excitonic models is also qualitatively different. In the former, the $U \gg t$ limit of Eq. (7) gives $c_{\text{SW}}=\sqrt{2}J$

where $J=4t^2/U$ is the exchange integral of the corresponding effective Heisenberg model.[48–50] In the excitonic model, however, the inset of Fig. 10(a) reveals that c_{SW} has only weak dependence upon the interaction strength for $g_{\mathrm{SDW}} \gg t$. A strong-coupling expansion of Eq. (38) gives the limiting value $c_{\mathrm{SW}}=\sqrt{2}ta$. The interpretation of the strong-coupling limit in the excitonic model is not straightforward: as $g_{\mathrm{SDW}} \to \infty$, simultaneous occupation of the c and f states on the same site is forbidden but double occupation of the c and f states is allowed. Since we work at half filling, one might expect a checkerboard orbital ordering with filled c states on one sublattice and filled f states on the other, which is incompatible with SDW order. However, it has been shown in a *spinless* two-band model that such a state is unstable toward an excitonic insulator or a phase with either the c or f states fully occupied for $\epsilon_0 \neq 0$.[53] How this result would change in the presence of spin is not clear. In any case, the $g_{\mathrm{SDW}} \gg t$ limit seems somewhat unphysical without also considering g_{cc} and g_{ff} to be large and so we do not further discuss the strong-coupling regime here.

The evaluation of the intraband susceptibilities proceeds similarly but here the denominator is $\mathcal{D}(\mathbf{q}+\mathbf{Q},\omega)$. This yields an identical spin-wave dispersion but shifted to $\mathbf{q}=0$. As in the Hubbard model, however, the spin wave has vanishing weight close to the zone center and is barely visible as it exits the continuum in the lower right-hand corner of Fig. 7(b).

B. Metallic SDW state

It is more generally the case that the nesting condition $\epsilon^c_{\mathbf{k}} \approx -\epsilon^f_{\mathbf{k}+\mathbf{Q}}$ is only approximately satisfied. Furthermore, there may be portions of the Fermi surface that do not participate in the excitonic instability, as is the case in chromium.[24–26] The pnictides also have a complicated Fermi surface involving several bands. Although the numerous models for the band structure differ in their details,[12,13,15,36–40] there is general agreement that in the "unfolded" Brillouin zone corresponding to the 2D iron sublattice the nesting of hole pockets at $\mathbf{k}=(0,0)$ with electron pockets at $(\pi/a,0)$ or $(0,\pi/a)$ is primarily responsible for the SDW. In the physical, tetragonal Brillouin zone, both $(\pi/a,0)$ and $(0,\pi/a)$ are folded back onto the M point, leading to two electron pockets around that point.[36,40] The wave vectors in the present paper refer to the unfolded zone. Apparently only one of the electron pockets undergoes the excitonic instability, yielding a SDW with ordering vector $\mathbf{Q}=(\pi/a,0)$, say. The other electron pocket at $\mathbf{Q}'=(0,\pi/a)$ remains ungapped. We can capture the basic features of this scenario within a two-band model by including one hole pocket around (0,0) and treating the two electron pockets as belonging to the same band. We thus assume the band structure

$$\epsilon^c_{\mathbf{k}} = 2t \cos k_x a \cos k_y a + \epsilon_c, \tag{43a}$$

$$\epsilon^f_{\mathbf{k}} = 2t(\cos k_x a + \cos k_y a) + \epsilon_f. \tag{43b}$$

We take $t=1$ eV, $\epsilon_c=1.5$ eV, $\epsilon_f=-3.5$ eV, and fix the doping at $n=1.916$, which gives electron and hole pockets of identical area. The band structure and Fermi surface are illustrated in Figs. 11(a) and 11(b), respectively. Note that the hole pocket is nearly but not quite perfectly nested with both electron pockets. We impose a single-$\mathbf{Q}$ SDW with ordering vector $\mathbf{Q}=(\pi/a,0)$. For $g_{\mathrm{SDW}}=1.873$ eV we find a mean-field state with critical temperature $T_{\mathrm{SDW}}=132$ K and $T=0$ gap $\Delta=21.3$ meV. In the $T=0$ SDW state both the hole pocket at the zone center and the electron pocket at $(\pi/a,0)$ are completely gapped while the electron pocket at $(0,\pi/a)$ remains intact.

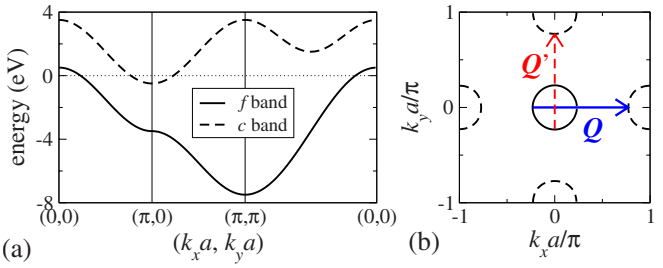

FIG. 11. (Color online) (a) Band structure and (b) Fermi surface of the noninteracting metallic excitonic model. In (b), the nesting vectors $\mathbf{Q}=(\pi/a,0)$ and $\mathbf{Q}'=(0,\pi/a)$ are also shown.

The imaginary parts of the interband, intraband, and total transverse susceptibilities for $\mathbf{q}=(q_x,0)$ are shown in Figs. 12(a)–12(c), respectively. Our results are very similar to those for the insulating SDW model in Fig. 7. The slightly higher magnitude of the transverse susceptibility is due to the greater density of states in the electronlike band. The similarity is not surprising, as the relevant excitations in both models have identical origin, i.e., excitations between states close to two Fermi pockets which are gapped by an excitonic SDW instability. The states close to the ungapped Fermi pocket do not contribute to the interband susceptibility for the plotted range of $(\mathbf{q},\omega)$. Although these states do contribute to the intraband susceptibility for small values of $\mathbf{q}$, they are only negligibly mixed with states in the holelike band and thus are not RPA enhanced by the interband interactions.

In contrast to the insulating SDW state studied in Sec. III A, here the interband susceptibility does not just depend on $|\delta\mathbf{q}|$: although it is identical for $\mathbf{q}=(q_x,0)$ and $(\pi/a,\pi/a-q_x)$ by tetragonal symmetry, and quantitatively very similar along $\mathbf{q}=(\pi/a-q_x/\sqrt{2},\pm q_x/\sqrt{2})$, away from these high-symmetry lines in $\mathbf{q}$ space we find that the continuum can extend to significantly lower energies. This is shown in Fig. 13, where we plot $\mathrm{Im}\,\chi^{\mathrm{inter}}_{-+}(\mathbf{q},\omega)$ for $\mathbf{q}=(\pi/a-\tilde{q}\cos\theta,\tilde{q}\sin\theta)$ with $\theta=\pi/8$. Although the response for $\omega>100$ meV is very similar to that in Fig. 12(a), we see that the lower edge of the continuum is not constant at $\omega=2\Delta$ but instead shows higher and lower thresholds which coincide only at special values of $\mathbf{q}$.

The origin of this threshold behavior is the imperfect nesting of the Fermi pockets. Consider Fig. 14(a), which shows the superimposed hole and back-folded electron Fermi pockets: along $\mathbf{k}=(k_x,0)$ or $(0,k_y)$, the width of the hole Fermi pocket is greater than that of the electron one while the reverse is true for $\mathbf{k}=(k_x,k_y=k_x)$ or $(k_x,k_y=-k_x)$. In the former case, the intersection of the noninteracting electronlike and holelike dispersions therefore occurs above the Fermi energy

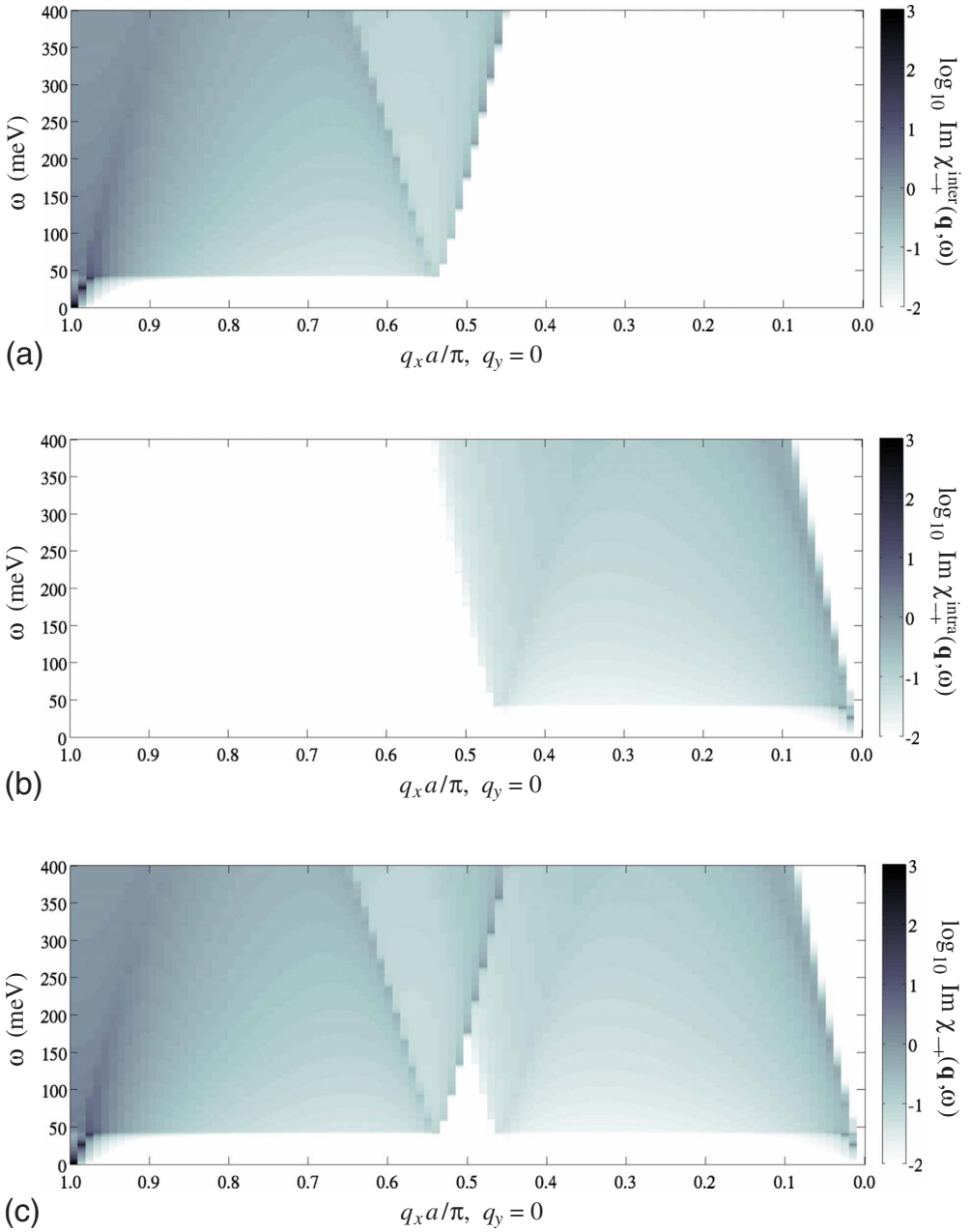

FIG. 12. (Color online) Imaginary part of the (a) interband, (b) intraband, and (c) total transverse susceptibility in the metallic excitonic model for $\mathbf{q}=(q_x,0)$. The spin-wave dispersion is visible as the dark line at $\omega<2\Delta$ close to $\mathbf{Q}$ in (a) and (c). Note the logarithmic color scale.

[Fig. 14(c)] while in the latter it occurs below the Fermi energy [Fig. 14(d)]. In the reconstructed bands of the excitonic model, the SDW gap is always centered at the point of intersection of the original bands, as can be seen from Eq. (26) and in Figs. 14(c) and 14(d). In general, the difference between the Fermi energy and the bottom of the reconstructed electronlike band, $\Delta_{+,\mathbf{k}}$, and the difference between the Fermi energy and the top of the reconstructed holelike band, $\Delta_{-,\mathbf{k}}$, will be unequal. The minimum energy for an interband excitation with wave vector $\mathbf{Q}+\delta\mathbf{q}$ is therefore $\min_{\mathbf{k}}(\Delta_{\pm,\mathbf{k}}+\Delta_{\mp,\mathbf{k}+\delta\mathbf{q}})$. For $\delta\mathbf{q}$ along the high-symmetry directions mentioned above, the tetragonal symmetry of the Fermi pockets ensures that this minimum energy is 2Δ. Away from these directions, however, the energy difference depends on $\delta\mathbf{q}$. For example, the states near the Fermi surface in Fig. 14(a) at $\mathbf{k}=(0,k_y)$ and $(k_x,k_y=k_x)$ are connected by $\delta\mathbf{q}=[\tilde{q}\cos(\pi/8),-\tilde{q}\sin(\pi/8)]$ with $\tilde{q}=0.17\pi/a$; from Figs. 14(c) and 14(d) we see that the minimum energy for single-particle excitations with this wave vector is $1.2\Delta=25.6$ meV, which marks the lowest edge of the continuum in Fig. 13. The upper threshold originates from the maximum energy connecting the top of the holelike band and the bottom of the electronlike band, which for this $\mathbf{q}$ is $2.8\Delta=59.6$ meV. For the remainder of this paper we shall restrict ourselves to high-symmetry directions.

Since only one-electron pocket is gapped, the directions $(q_x,0)$ and $(0,q_y)$ are not equivalent. The imaginary part of the interband transverse susceptibility along $\mathbf{q}=(0,q_y)$ is

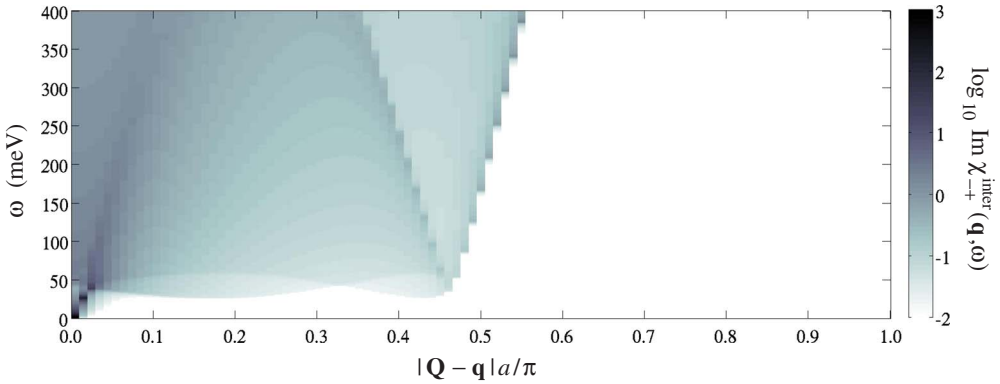

FIG. 13. (Color online) Imaginary part of the interband transverse susceptibility in the metallic excitonic model for $\mathbf{q}=(\pi/a-\tilde{q}\cos\theta,\tilde{q}\sin\theta)$ for $\theta=\pi/8$. The spin-wave dispersion is visible as the dark line at $\omega<2\Delta$ close to $\mathbf{Q}$. Note the logarithmic color scale.

shown in Fig. 15. This is the direction toward the second nesting vector $\mathbf{Q}'=(0,\pi/a)$, which was not selected by the SDW instability. For $\mathbf{q}$ sufficiently close to $\mathbf{Q}'$, we thus find the response generated by transitions between states near the (gapped) hole Fermi pocket and states near the ungapped electron Fermi pocket. At $\omega\gtrsim 2\Delta$, this is very similar to the interband susceptibility near $\mathbf{Q}$ [Fig. 12(a)], reflecting the small changes to the band structure at high energies upon opening of the SDW gap. The differences are more striking at lower energies. In particular, comparing Fig. 15 to Fig. 12(a), we see that the continuum extends to lower energies close to $\mathbf{Q}'$ than close to $\mathbf{Q}$. The minimum energy required for a single-particle excitation between the states near the ungapped electron pocket and the gapped hole pocket is smaller than 2Δ, thus giving a lower threshold for the continuum near $\mathbf{Q}'$.

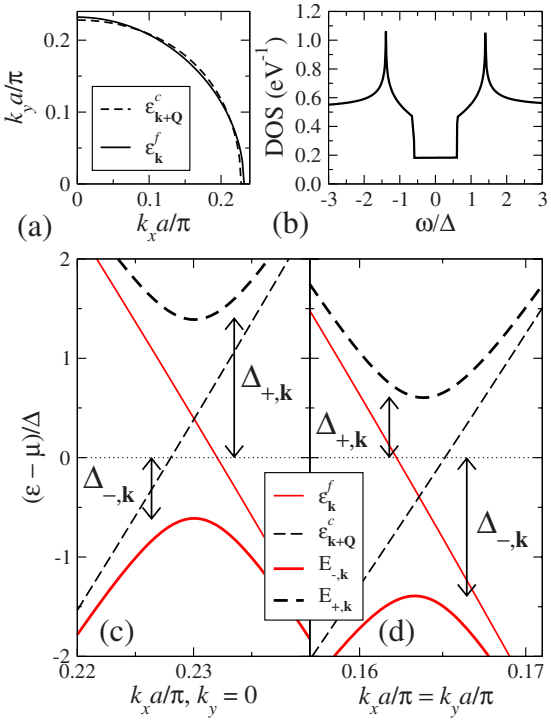

FIG. 14. (Color online) (a) Electron and hole Fermi pockets superimposed upon one another. (b) Density of states close to the Fermi energy. (c) Comparison of the band structure near the intersection of $\epsilon^c_{\mathbf{k}+\mathbf{Q}}$ and $\epsilon^f_{\mathbf{k}}$ in the normal and SDW phases for $\mathbf{k}=(k_x,0)$. (d) Same as in (c) but for $\mathbf{k}=(k_x,k_y=k_x)$.

Another significant difference concerns the spin-wave dispersion. The spin-wave dispersion near $\mathbf{Q}$ is visible in the lower left-hand corner of Fig. 12(a), and it intersects the continuum and appears to continue as a paramagnon. From Fig. 15, we see that there is also a gapless Goldstone mode at $\mathbf{q}=\mathbf{Q}'$. This mode is gapless since it rotates the single-$\mathbf{Q}$ SDW into a superposition of $\mathbf{Q}$ and $\mathbf{Q}'$ SDWs, which is degenerate with the single-$\mathbf{Q}$ SDW in our tetragonal model. Although there appears to be a spin-wave branch around $\mathbf{Q}'$, it is not as distinct as in Fig. 12(a) due to the lower threshold of the continuum. We therefore plot the interband transverse susceptibilities for a finer $\mathbf{q}$ resolution near $\mathbf{Q}$ and $\mathbf{Q}'$ in Figs. 16(a) and 16(b), respectively. As expected from the discussion above, the former is qualitatively identical to Fig. 9. The latter, in contrast, shows several different features: the spin-wave dispersion does not curve away from the edge of the continuum but rather intersects it with little change in velocity and the spin-wave and paramagnon features approach much closer to one another than for $\mathbf{q}\approx\mathbf{Q}$. Although it is not clear from Fig. 16(b), the spin-wave and paramagnon dispersions do not intersect, and the spin waves become damped at $\omega\approx 1.7\Delta$.

To obtain the spin-wave dispersion, we must again solve $\mathrm{Re}\,\mathcal{D}(\mathbf{q},\omega)=0$ with $\mathcal{D}(\mathbf{q},\omega)$ given by Eq. (37). We have not been able to obtain analytical expressions for the spin-wave velocity, however, as the Fermi distribution functions appearing in the mean-field susceptibilities cannot be expanded as a Taylor series in $\delta\mathbf{q}$ due to the ungapped electron Fermi pocket. Plotting the dispersions at $\mathbf{q}\approx\mathbf{Q}$ and $\mathbf{q}\approx\mathbf{Q}'$ in Fig. 17, we see that the velocity at $\mathbf{Q}$ is roughly 25% higher than at $\mathbf{Q}'$. Despite the variation in $\Delta_{\pm,\mathbf{k}}$, there is no anisotropy of the low-energy spin-wave velocity. The difference between the results for $\theta=0$ and $\theta=\pi/8$ at higher energies is due to the lower edge of the continuum in the latter case. Whereas the spin waves close to $\mathbf{Q}$ have a very similar dispersion compared to the insulating model [Fig. 10(b)], the dispersion close to $\mathbf{Q}'$ has two noticeable kinks at $\omega=0.65\Delta$ and $\omega=1.25\Delta$. As shown in the inset, these kinks coincide with abrupt changes in $\mathrm{Im}\,\mathcal{D}(\mathbf{q},\omega)$: $\mathrm{Im}\,\mathcal{D}(\mathbf{q},\omega)$ becomes finite at $\omega=0.65\Delta$ and starts to sharply increase at $\omega=1.25\Delta$. The first feature corresponds to the onset of Landau damping as

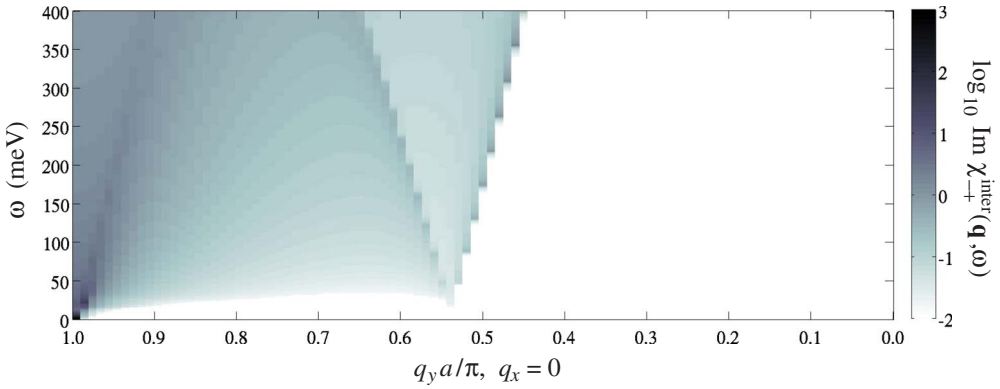

FIG. 15. (Color online) Imaginary part of the interband transverse susceptibility in the metallic excitonic model for $\mathbf{q}=(0,q_y)$. The spin-wave dispersion is visible as the dark line at $\omega<2\Delta$ close to $\mathbf{Q}'$ ($q_y=0$). Note the logarithmic color scale.

the spin-wave branch enters the continuum. The second feature is a result of the DOS, as discussed in the following paragraph.

Examining the lower edge of the continuum in both panels of Fig. 16, we see that whereas the continuum disappears sharply at $\omega=2\Delta$ near $\mathbf{Q}$, it appears to vanish more smoothly near $\mathbf{Q}'$. In the latter case there are two distinct thresholds, which are particularly visible around $q_y=0.99\pi/a$. To examine this more closely, we plot Im $\chi_{-+}(\mathbf{q},\omega)$ as a function of ω for fixed $\mathbf{q}$ near $\mathbf{Q}$ and $\mathbf{Q}'$ in Figs. 18(a) and 18(b), respectively. In the former case, we see the steplike start of the continuum at $\omega=2\Delta$. The peak at this energy is due both to the remnant of the spin-wave branch (at least for $q_x=0.98\pi/a$) and to the enhancement of the DOS at the edge of the SDW gap. The finite value of Im $\chi_{-+}(\mathbf{q},\omega)$ for $\omega<2\Delta$ is an artifact of the finite width δ. The susceptibility near $\mathbf{Q}'$ is qualitatively different: the lower threshold of the continuum is at $\omega_1=0.65\Delta$ and immediately above this the susceptibility increases continuously as $\sqrt{\omega-\omega_1}$. At $\omega_2=1.3\Delta$, the susceptibilility abruptly starts to increase more steeply. The locations of these two thresholds correspond to the kinks in the spin-wave dispersion. The rapid increase in Im $\chi_{-+}(\mathbf{q},\omega)$ above ω_2 accounts for the strong increase in the damping (see inset of Fig. 17).

As for the interband susceptibility near $\mathbf{Q}$, the origin of the lower threshold is the variation in $\Delta_{\pm,\mathbf{k}}$. The difference is

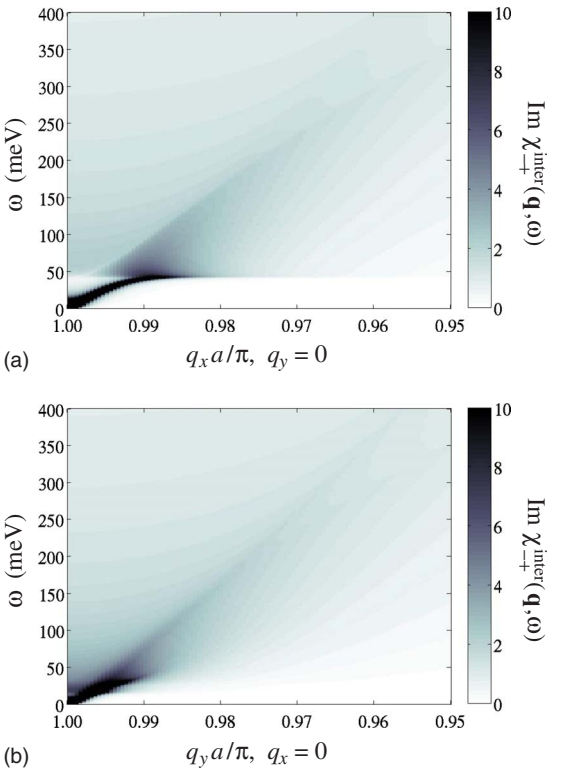

FIG. 16. (Color online) Imaginary part of the interband transverse susceptibility in the metallic excitonic model for (a) $\mathbf{q}=(q_x,0)$ close to $\mathbf{Q}$ and (b) $\mathbf{q}=(0,q_y)$ close to $\mathbf{Q}'$. In both panels the spin-wave dispersion is visible as the thick black line in the bottom left-hand corner. Note that in (b) that the continuum region starts at $\omega\approx 0.6\Delta$. In both panels we use a linear color scale.

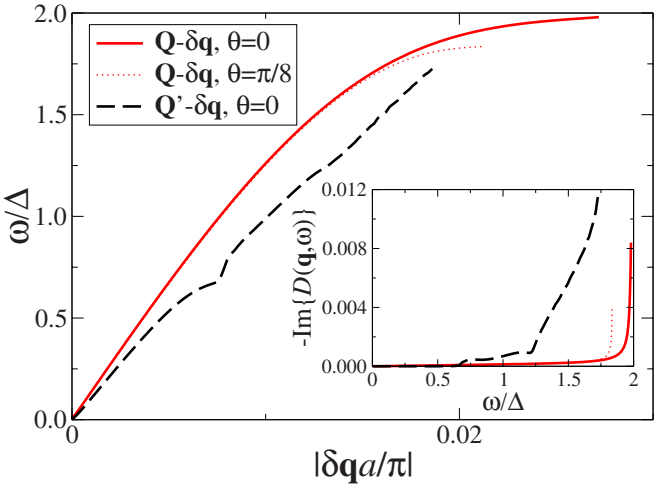

FIG. 17. (Color online) Spin-wave dispersion in the metallic excitonic model close to $\mathbf{Q}$ for $\delta\mathbf{q}=(-\tilde{q}\cos\theta,\tilde{q}\sin\theta)$ with $\theta=0$ (solid red line) and $\theta=\pi/8$ (thin dotted red line). The dispersion for $\theta=\pi/4$ is indistinguishable from the $\theta=0$ case. We also plot the spin-wave dispersion close to $\mathbf{Q}'$ (dashed black line). Inset: imaginary part of $\mathcal{D}(\mathbf{q},\omega)$ for each dispersion. We have used a 20 000 $\times$ 20 000 $\mathbf{k}$-point mesh and a width $\delta=0.1$ meV to calculate the mean-field susceptibilities. Note that the finite value of Im $\mathcal{D}(\mathbf{q},\omega)$ for the spin waves close to $\mathbf{Q}$ for $\omega<2\Delta$ is an artifact of the finite width δ.

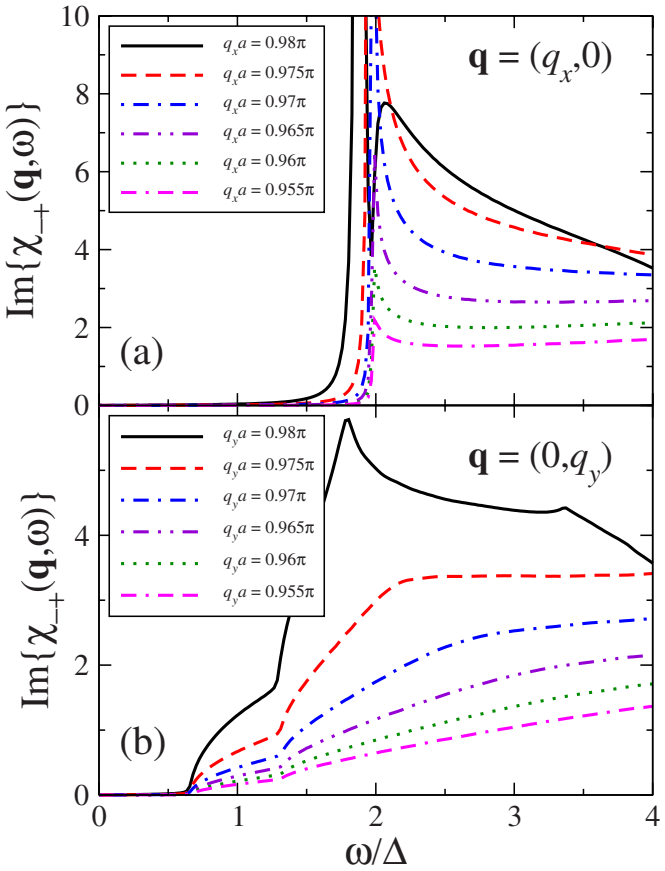

FIG. 18. (Color online) Imaginary part of the transverse susceptibility as a function of ω at various values of $\mathbf{q}$ near (a) $\mathbf{Q}$ and (b) $\mathbf{Q}'$ in the metallic excitonic model. We have calculated the mean-field susceptibilities using a $30\,000 \times 30\,000$ $\mathbf{k}$-point mesh and a width $\delta = 0.2$ meV.

that here the threshold originates from the minimum energy required for a single-particle excitation between the states near the gapped hole pocket and the states near the ungapped electron pocket, $\omega_1 = \min_{\mathbf{k}}(\Delta_{+,\mathbf{k}}, \Delta_{-,\mathbf{k}})$. From Figs. 14(c) and 14(d) we deduce $\omega_1 \approx 0.6\Delta$, closely matching the lower threshold in Fig. 18(b). The strong increase in Im $\chi_{-+}(\mathbf{q},\omega)$ above ω_2 is due to the peaks in the DOS located at $\pm\omega_2$ on either side of the Fermi energy, shown in Fig. 14(b) because of this DOS enhancement, the density of excitations between states close to the gapped and ungapped Fermi pockets is increased above ω_2.

IV. EXPERIMENTAL SITUATION

This work ultimately aims to shed light upon the nature of the antiferromagnetism in the iron pnictides, in particular, the extent to which it is itinerant or localized in character. There are several published results of inelastic neutron scattering examining the spin excitations in the antiferromagnetic state of $CaFe_2As_2$,[47,54,55] $SrFe_2As_2$,[56] and $BaFe_2As_2$.[46,57] In these experiments, only transverse excitations contribute to the neutron-scattering cross section, allowing us to write it as

$$\frac{d^2\sigma}{d\Omega dE} \propto |F(\mathbf{q})|^2 [n_B(\omega) + 1] \mathrm{Im}\, \chi_{-+}(\mathbf{q},\omega), \qquad (44)$$

where $F(\mathbf{q})$ is a form factor and $n_B(\omega)$ is the Bose-Einstein distribution function. A direct, quantitative comparison between theory and experiment would require a more realistic model for the low-energy band structure than the one we are using. We nevertheless make several general remarks relating what we have learnt about the spin excitations in the excitonic SDW state to the experimental results.

We first review the experimental situation. Despite considerable variation in the Néel temperature within the AFe_2As_2 (A=Ca, Sr, or Ba) family, the static magnetic properties of these compounds are rather similar. In particular, antiferromagnetism only occurs in the presence of an orthorhombic distortion, which fixes the ordering vector $\mathbf{Q}$. Experiments on the low-energy spin dynamics are also in broad agreement: there is a strongly dispersing spin wave close to $\mathbf{Q}$,[46,47,54–57] the spin-wave velocity is anisotropic,[47,54–57] and the spin-wave dispersion has a gap of energy 6–10 meV.[46,47,54–57] At present, however, there is considerable disagreement over the high-energy excitations. For $CaFe_2As_2$, it was reported[55] that the spin wave is strongly damped at energies above 100 meV, suggesting the presence of a particle-hole continuum. On the other hand, although Zhao *et al.*[47] found similar spin-wave velocities, they did not observe any significant jump in the damping of the spin wave below 200 meV, which would indicate the intersection of the spin-wave dispersion with the continuum. The results for $BaFe_2As_2$ show greater inconsistency, with reports[46] of strong spin excitations possibly up to 170 meV in stark disagreement with claims of spin-wave damping by continuum excitations at energies as low as 24 meV.[57]

The results of Refs. 57 and 55 are most consistent with itinerant antiferromagnetism, as the existence of a particle-hole continuum is a key feature of this scenario. Interpreting the latter experiment[55] in terms of the excitonic model, we deduce a SDW gap of $\Delta \approx 50$ meV. This is nearly twice the estimate $\Delta \approx 30$ meV of the $T=0$ gap based on ARPES for $SrFe_2As_2$.[20] Although a SDW gap of only 12 meV for $BaFe_2As_2$, which we could infer from Ref. 57, seems low, we have seen above that spin-wave damping sets in at energies much smaller than 2Δ, depending upon the details of the reconstructed band structure. In order to fit the results of Ref. 47 into the excitonic picture, however, we require a SDW gap of at least 100 meV implying a rather high value of the ratio $\Delta/k_B T_{\mathrm{SDW}} \gtrsim 7$. These results instead support a local-moment picture.[11,41–43] The absence of the continuum is nevertheless surprising since ARPES shows clear evidence for quasiparticle bands at low energies, which suggests a possible resolution:[20,58] the imperfect nesting of the elliptical electron pockets with the circular hole pocket is expected to yield incompletely gapped Fermi surfaces in the SDW state, which implies that continuum excitations are present down to zero energy. As such, the spin waves would be damped at all energies and the jump in the damping characteristic of the entry into the continuum is absent. Such an explanation is of

course at odds with Ref. 55, indicating the need for further work to clarify the experimental situation.

The reported 40% anisotropy of the spin-wave velocity within the *ab* plane[47,55] is quite remarkable. Although this effect is absent from our results due to the tetragonal symmetry of the Fermi pockets, it nevertheless seems rather too large to be accounted for by the expected elliptical shape of the electronlike Fermi pockets in the pnictides.[47] Experimental results also do not show a second spin-wave branch at $\mathbf{Q}'$, as found here for the metallic SDW model. Both observations are likely due to the orthorhombic distortion in the SDW phase, which lifts the degeneracy of the $(\pi,0)$ and $(0,\pi)$ SDW,[36] and do not imply a failure of the excitonic scenario.

We finally remark upon the gap in the spin-wave dispersion in the pnictides. Due to the absence of magnetic anisotropy is our model, we always find Goldstone modes in the SDW phase. As demonstrated in Fishman and Liu's study of manganese alloys,[27] a gap is possible in an excitonic SDW state in the presence of magnetoelastic coupling. The magnetoelastic coupling in the pnictides is indeed strong, as evidenced by the role of the orthorhombic distortion in fixing the polarization and the ordering vector of the SDW,[6,7,57] suggesting that it might be responsible for the spin-wave gap.

In summary, the neutron-scattering data for the antiferromagnetic state in the pnictides are currently unable to decide upon the origin and character of the magnetism. We have shown that the excitonic SDW scenario gives spin-wave excitations in qualitative agreement with experiments. An obvious direction of future work is therefore to examine the spin excitations based on more realistic band structures. Considering the imperfect nesting of the electron and hole pockets in the pnictides, it will be particularly interesting to address the possibility of incommensurate SDW order.[34] The effects of the interactions not directly contributing to the SDW instability should be included. Comparison of our results with those obtained within a model explicitly accounting for the orbital character of the bands is also important. Furthermore, the orthorhombic distortion and a magnetoelastic coupling should be implemented for greater realism. Although the spin excitations in more sophisticated models will differ in their details from those presented here, we nevertheless think that our results will remain qualitatively correct and will thus be valuable in interpreting future experiments.

V. SUMMARY

We have presented an analysis of the zero-temperature transverse spin excitations in the excitonic SDW state of two-band 2D models with nested electronlike and holelike Fermi pockets. Using the RPA, we have derived the Dyson equation for the spin susceptibility and have shown that the total spin susceptibility can be divided into contributions from interband and intraband excitations. We have solved the Dyson equation in the special case when only the interactions responsible for the SDW are nonzero. While the interband excitations are then directly enhanced by the interactions, the intraband excitations are still indirectly enhanced due to the mixing of the electronlike and holelike states in the SDW phase. The susceptibility exhibits collective spin-wave branches close to the SDW ordering vector $\mathbf{Q}$ and also, with much smaller weight, close to $\mathbf{q}=0$, as well as a continuum of single-particle excitations at energies above a threshold on the order of the SDW gap.

Depending upon the noninteracting band structure, the opening of the excitonic gap can result in qualitatively different SDW states. This has been illustrated by considering two models, one which becomes insulating in the SDW state and another which remains metallic due to the presence of an ungapped portion of the Fermi surface. For comparison, we have also performed the corresponding calculations for a 2D Hubbard model with the same mean-field SDW gap. Differences in the spin excitations between the insulating and metallic models occur only at low energies and mainly close to the nesting vector $\mathbf{Q}'$ between the (gapped) hole pocket and the ungapped electron pocket, which is essentially unaffected by the SDW formation. We have also discussed data from neutron-scattering experiments in light of our results. We conclude that the available data do not yet allow us to distinguish between an excitonic SDW and a local-moment scenario for the antiferromagnetic order in the pnictides.

*brydon@theory.phy.tu-dresden.de
†carsten.timm@tu-dresden.de

[1] Y. Kamihara, T. Watanabe, M. Hirano, and H. Hosono, J. Am. Chem. Soc. **130**, 3296 (2008).
[2] M. Rotter, M. Tegel, and D. Johrendt, Phys. Rev. Lett. **101**, 107006 (2008).
[3] Z.-A. Ren, W. Lu, J. Yang, W. Yi, X.-L. Shen, Z.-C. Li, G.-C. Che, X.-L. Dong, L.-L. Sun, F. Zhou, and Z.-X. Zhao, Chin. Phys. Lett. **25**, 2215 (2008).
[4] J. W. Lynn and P. Dai, Physica C **469**, 469 (2009).
[5] C. de la Cruz, Q. Huang, J. W. Lynn, J. Li, W. Ratcliff II, J. L. Zarestky, H. A. Mook, G. F. Chen, J. L. Luo, N. L. Wang, and P. Dai, Nature (London) **453**, 899 (2008).
[6] J. Zhao, Q. Huang, C. de la Cruz, S. Li, J. W. Lynn, Y. Chen, M. A. Green, G. F. Chen, G. Li, Z. Li, J. L. Luo, N. L. Wang, and P. Dai, Nature Mater. **7**, 953 (2008); J. Zhao, Q. Huang, C. de la Cruz, J. W. Lynn, M. D. Lumsden, Z. A. Ren, J. Yang, X. Shen, X. Dong, Z. Zhao, and P. Dai, Phys. Rev. B **78**, 132504 (2008).
[7] Q. Huang, Y. Qiu, W. Bao, M. A. Green, J. W. Lynn, Y. C. Gasparovic, T. Wu, G. Wu, and X. H. Chen, Phys. Rev. Lett. **101**, 257003 (2008); A. Jesche, N. Caroca-Canales, H. Rosner, H. Borrmann, A. Ormeci, D. Kasinathan, H. H. Klauss, H. Luetkens, R. Khasanov, A. Amato, A. Hoser, K. Kaneko, C. Krellner, and C. Geibel, Phys. Rev. B **78**, 180504(R) (2008).
[8] H. Luetkens, H.-H. Klauss, M. Kraken, F. J. Litterst, T. Dellmann, R. Klingeler, C. Hess, R. Khasanov, A. Amato, C. Baines, M. Kosmala, O. J. Schumann, M. Braden, J. Hamann-Borrero, N. Leps, A. Kondrat, G. Behr, J. Werner, and B. Büchner, Na-

ture Mater. **8**, 305 (2009).
[9] G. Mu, X.-Y. Zhu, L. Fang, L. Shan, C. Ren, and H.-H. Wen, Chin. Phys. Lett. **25**, 2221 (2008).
[10] L. Shan, Y. Wang, X. Zhu, G. Mu, L. Fang, C. Ren, and H.-H. Wen, EPL **83**, 57004 (2008).
[11] Q. Si and E. Abrahams, Phys. Rev. Lett. **101**, 076401 (2008).
[12] K. Kuroki, S. Onari, R. Arita, H. Usui, Y. Tanaka, H. Kontani, and H. Aoki, Phys. Rev. Lett. **101**, 087004 (2008).
[13] M. M. Korshunov and I. Eremin, Phys. Rev. B **78**, 140509(R) (2008).
[14] P. A. Lee, N. Nagaosa, and X.-G. Wen, Rev. Mod. Phys. **78**, 17 (2006).
[15] D. J. Singh and M.-H. Du, Phys. Rev. Lett. **100**, 237003 (2008); I. I. Mazin, D. J. Singh, M. D. Johannes, and M. H. Du, *ibid.* **101**, 057003 (2008).
[16] M. A. McGuire, A. D. Christianson, A. S. Sefat, B. C. Sales, M. D. Lumsden, R. Jin, E. A. Payzant, D. Mandrus, Y. Luan, V. Keppens, V. Varadarajan, J. W. Brill, R. P. Hermann, M. T. Sougrati, F. Grandjean, and G. J. Long, Phys. Rev. B **78**, 094517 (2008); M. A. McGuire, R. P. Hermann, A. S. Sefat, B. C. Sales, R. Jin, D. Mandrus, F. Grandjean, and G. J. Long, New J. Phys. **11**, 025011 (2009).
[17] R. H. Liu, G. Wu, T. Wu, D. F. Fang, H. Chen, S. Y. Li, K. Liu, Y. L. Xie, X. F. Wang, R. L. Yang, L. Ding, C. He, D. L. Feng, and X. H. Chen, Phys. Rev. Lett. **101**, 087001 (2008).
[18] J. K. Dong, L. Ding, H. Wang, X. F. Wang, T. Wu, G. Wu, X. H. Chen, and S. Y. Li, New J. Phys. **10**, 123031 (2008).
[19] S. E. Sebastian, J. Gillett, N. Harrison, P. H. C. Lau, C. H. Mielke, and G. G. Lonzarich, J. Phys.: Condens. Matter **20**, 422203 (2008); J. G. Analytis, R. D. McDonald, J.-H. Chu, S. C. Riggs, A. F. Bangura, C. Kucharczyk, M. Johannes, and I. R. Fisher, Phys. Rev. B **80**, 064507 (2009).
[20] D. Hsieh, Y. Xia, L. Wray, D. Qian, K. Gomes, A. Yazdani, G. F. Chen, J. L. Luo, N. L. Wang, and M. Z. Hasan, arXiv:0812.2289 (unpublished).
[21] L. Boeri, O. V. Dolgov, and A. A. Golubov, Phys. Rev. Lett. **101**, 026403 (2008); Physica C **469**, 628 (2009).
[22] P. A. Fedders and P. C. Martin, Phys. Rev. **143**, 245 (1966).
[23] S. H. Liu, Phys. Rev. B **2**, 2664 (1970).
[24] T. M. Rice, Phys. Rev. B **2**, 3619 (1970).
[25] N. I. Kulikov and V. V. Tugushev, Sov. Phys. Usp. **27**, 954 (1984).
[26] E. Fawcett, Rev. Mod. Phys. **60**, 209 (1988); E. Fawcett, H. L. Alberts, V. Y. Galkin, D. R. Noakes, and J. V. Yakhmi, *ibid.* **66**, 25 (1994).
[27] R. S. Fishman and S. H. Liu, Phys. Rev. B **58**, R5912 (1998); Phys. Rev. B **59**, 8672 (1999); **59**, 8681 (1999).
[28] L. V. Keldysh and Y. V. Kopaev, Sov. Phys. Solid State **6**, 2219 (1965); J. des Cloizeaux, J. Phys. Chem. Solids **26**, 259 (1965); D. Jérome, T. M. Rice, and W. Kohn, Phys. Rev. **158**, 462 (1967).
[29] B. A. Volkov, Y. V. Kopaev, and A. I. Rusinov, Sov. Phys. JETP **41**, 952 (1976).
[30] D. W. Buker, Phys. Rev. B **24**, 5713 (1981).
[31] A. V. Chubukov, D. V. Efremov, and I. Eremin, Phys. Rev. B **78**, 134512 (2008).
[32] Q. Han, Y. Chen, and Z. D. Wang, EPL **82**, 37007 (2008).
[33] T. Mizokawa, T. Sudayama, and Y. Wakisaka, J. Phys. Soc. Jpn. Suppl. C **77**, 158 (2008).
[34] V. Cvetkovic and Z. Tesanovic, EPL **85**, 37002 (2009); Phys. Rev. B **80**, 024512 (2009).
[35] A. B. Vorontsov, M. G. Vavilov, and A. V. Chubukov, Phys. Rev. B **79**, 060508(R) (2009).
[36] P. M. R. Brydon and C. Timm, Phys. Rev. B **79**, 180504(R) (2009).
[37] S. Raghu, X.-L. Qi, C.-X. Liu, D. J. Scalapino, and S.-C. Zhang, Phys. Rev. B **77**, 220503(R) (2008).
[38] J. Lorenzana, G. Seibold, C. Ortix, and M. Grilli, Phys. Rev. Lett. **101**, 186402 (2008).
[39] Y. Ran, F. Wang, H. Zhai, A. Vishwanath, and D.-H. Lee, Phys. Rev. B **79**, 014505 (2009).
[40] R. Yu, K. T. Trinh, A. Moreo, M. Daghofer, J. A. Riera, S. Haas, and E. Dagotto, Phys. Rev. B **79**, 104510 (2009).
[41] T. Yildirim, Phys. Rev. Lett. **101**, 057010 (2008).
[42] G. S. Uhrig, M. Holt, J. Oitmaa, O. P. Sushkov, and R. R. P. Singh, Phys. Rev. B **79**, 092416 (2009).
[43] F. Krüger, S. Kumar, J. Zaanen, and J. van den Brink, Phys. Rev. B **79**, 054504 (2009).
[44] T. Kroll, S. Bonhommeau, T. Kachel, H. A. Dürr, J. Werner, G. Behr, A. Koitzsch, R. Hübel, S. Leger, R. Schönfelder, A. K. Ariffin, R. Manzke, F. M. F. de Groot, J. Fink, H. Eschrig, B. Büchner, and M. Knupfer, Phys. Rev. B **78**, 220502(R) (2008).
[45] W. L. Yang, A. P. Sorini, C.-C. Chen, B. Moritz, W.-S. Lee, F. Vernay, P. Olalde-Velasco, J. D. Denlinger, B. Delley, J.-H. Chu, J. G. Analytis, I. R. Fisher, Z. A. Ren, J. Yang, W. Lu, Z. X. Zhao, J. van den Brink, Z. Hussain, Z.-X. Shen, and T. P. Devereaux, Phys. Rev. B **80**, 014508 (2009).
[46] R. A. Ewings, T. G. Perring, R. I. Bewley, T. Guidi, M. J. Pitcher, D. R. Parker, S. J. Clarke, and A. T. Boothroyd, Phys. Rev. B **78**, 220501(R) (2008).
[47] J. Zhao, D. T. Adroja, D.-X. Yao, R. Bewley, S. Li, X. F. Wang, G. Wu, X. H. Chen, J. Hu, and P. Dai, Nat. Phys. **5**, 555 (2009).
[48] J. R. Schrieffer, X. G. Wen, and S. C. Zhang, Phys. Rev. B **39**, 11663 (1989).
[49] A. Singh and Z. Tešanović, Phys. Rev. B **41**, 614 (1990).
[50] A. V. Chubukov and D. M. Frenkel, Phys. Rev. B **46**, 11884 (1992).
[51] P. W. Anderson, Phys. Rev. **86**, 694 (1952).
[52] H. Hasegawa, J. Low Temp. Phys. **31**, 475 (1978).
[53] C. D. Batista, Phys. Rev. Lett. **89**, 166403 (2002).
[54] R. J. McQueeney, S. O. Diallo, V. P. Antropov, G. D. Samolyuk, C. Broholm, N. Ni, S. Nandi, M. Yethiraj, J. L. Zarestky, J. J. Pulikkotil, A. Kreyssig, M. D. Lumsden, B. N. Harmon, P. C. Canfield, and A. I. Goldman, Phys. Rev. Lett. **101**, 227205 (2008).
[55] S. O. Diallo, V. P. Antropov, T. G. Perring, C. Broholm, J. J. Pulikkotil, N. Ni, S. L. Bud'ko, P. C. Canfield, A. Kreyssig, A. I. Goldman, and R. J. McQueeney, Phys. Rev. Lett. **102**, 187206 (2009).
[56] J. Zhao, D.-X. Yao, S. Li, T. Hong, Y. Chen, S. Chang, W. Ratcliff II, J. W. Lynn, H. A. Mook, G. F. Chen, J. L. Luo, N. L. Wang, E. W. Carlson, J. Hu, and P. Dai, Phys. Rev. Lett. **101**, 167203 (2008).
[57] K. Matan, R. Morinaga, K. Iida, and T. J. Sato, Phys. Rev. B **79**, 054526 (2009).
[58] D. H. Lu, M. Yi, S.-K. Mo, J. G. Analytis, J.-H. Chu, A. S. Erickson, D. J. Singh, Z. Hussain, T. H. Geballe, I. R. Fisher, and Z.-X. Shen, Physica C **469**, 452 (2009).